Eur. Phys. J. D (2016) 70: 251
DOI: 10.1140/epjd/e2016-70474-0

THE EUROPEAN PHYSICAL JOURNAL D

Topical Review

Non-equilibrium in low-temperature plasmas

Francesco Taccogna[a] and Giorgio Dilecce

CNR NANOTEC – PLasMI Lab, via Amendola 122/D, 70126 Bari, Italy

Received 26 July 2016 / Received in final form 4 October 2016
Published online 22 November 2016 –

Abstract. The wide range of applications of cold plasmas originates from their special characteristic of being a physical system out of thermodynamic equilibrium. This property enhances its reactivity at low gas temperature and allows to obtain macroscopic effects with a moderate energy consumption. In this review, the basic concepts of non-equilibrium in ionized gases are treated by showing why and how non-equilibrium functions of the degrees of freedom are formed in a variety of natural and man-made plasmas with particular emphasis on the progress made in the last decade. The modern point of view of a molecular basis of non-equilibrium and of a state-to-state kinetic approach is adopted. Computational and diagnostic techniques used to investigate the non-equilibrium conditions are also surveyed.

1 Introduction

The most important feature of 'cold' plasmas, roughly for electron temperature $T_e < 10$ eV, is that it can often be far from thermodynamic equilibrium. Such a condition allows efficient energy deposition into selected processes, like the production of active chemical species for different technological applications, minimizing thermal losses by operation at cold gas conditions. Investigation of low temperature plasmas requires a multidisciplinary approach. The way to couple input power with plasma is a typical electrical engineering problem, while the statistical description and electro-magnetic properties of the conductive gas is managed in a physics context, and the description of the chemical kinetics processes calls for a chemistry point of view. Thanks to the enormous number of applications, low temperature plasmas have embraced the knowledge of the most diverse branches of science such as astrophysics, biology, medicine, materials technology, etc. In this review we present the most important aspects of non-equilibrium in laboratory plasmas from a modern point of view, inviting the reader to overcome from the beginning the attitude at thinking that non-equilibrium is a small deviation from equilibrium, and to start from the idea that all the degrees of freedom must be described by distributions for which the equilibrium concept of temperature is almost never valid, and, mostly, will be used as a comfortable approximation. In particular, we aim at showing and make it clear that the energy input rates and redistribution among the degrees of freedom are the sources of non-equilibrium, and that both rely on the properties of atomic and molecular elementary processes. Some actual astrophysical and technological applications will be briefly described showing how non-equilibrium underlies their working principles. The paper is organized as follows. In Section 2 the basic concepts of non-equilibrium in ionized gases will be outlined; the non-equilibrium distribution functions of the different plasma components (electron, ion and neutral), correlated to peculiar cases, will be described in Section 3. Numerical modelling methodologies and diagnostic techniques will be outlined in Sections 7 and 8 respectively. It goes without saying, the subject is of enormous vastness, far beyond the possibility of being encompassed into a review. We have then chosen to give just a global overview in which only basic principles are presented, also through selected examples, and to address to few, most recent bibliographic references to advise and direct readers interested in going deep into single subjects. The selections operated in the paper reflect our personal history, since we have chosen to treat almost entirely issues in which we have had direct experience. We apologize for the uncountable amount of issues and references left out of this presentation.

2 Basics concepts in non-equilibrium ionized gases

The temperature is a quantity describing the average energy of a degree of freedom of a physical system. Its physical meaning, beyond the mere nature of a mathematical parameter, relies on the existence of an equilibrium condition. Equilibrium is a stationary concept, independent of time and of the time required to establish such a condition. The addition of an energy input to the system calls for the introduction of a kinetic point of view, in which the equilibrium concept starts to be an approximation linked to the characteristic time constants of the system: if the rate of energy input is much smaller than the rate of energy

[a] e-mail: francesco.taccogna@cnr.it

redistribution among all the degrees of freedom (from now on: energy transfer), we preserve the equilibrium concept giving it the name of quasi-equilibrium. Since the energy input can be a function of time and space, we can speak of local quasi-equilibrium: if the rate of change of the energy input is slow compared to the energy transfer, we get conditions of quasi-equilibrium at any point in space and at any time. It goes without saying, two ways are possible to increase the non-equilibrium degree: a) increase the energy input rate and its rate of change, b) decrease the energy transfer rates.

Partially ionized gas plasmas are a perfect field for achieving large non-equilibrium conditions. In almost all energy input cases, ranging from electric power, by application of electric fields, to photo-ionization by EUV to X-ray light, to cosmic radiation, the external energy is first coupled to electrons. The way light electrons transfer this energy to heavy atoms/molecules is strongly dependent on the kinetic energy. Elastic scattering, the most frequent and less energy dependent collision energy transfer, is very inefficient due to the very small – order of 10^5–10^{-4} – mass ratio of the colliders. Inelastic scattering, i.e. vibro-electronic excitation and ionization, is less frequent and strongly energy dependent, with energy thresholds up to a couple of tens of eV. As a result, the "thermal contact" between the electron and the heavy particles components is poor at low electron energies and better at high electron energies – the quantification of low and high depending on the gas composition – allowing electrons to easily gain energy up to inelastic processes thresholds and to transfer efficiently energy to vibrational, electronic excitations, ionization and dissociation. The mean energy hierarchy of the degrees of freedom, here reported for simplicity and historical reasons as a temperature hierarchy is:

$$T_e > T_v > T_{ion} \approx T_{rot} \approx T_0 \tag{1}$$

that reflects the hierarchy of the characteristic times of energy transfers between the different degrees of freedom. Electron temperatures T_e can easily be of the order of some eV (1 eV $\simeq$ 11 600 K), against a gas temperature T_0 close to the room one $\sim$300 K. The vibrational energy lying somewhere in between. This kind of partially ionized gases are referred to, in the literature, as non-thermal plasma (NTP) or low-temperature plasma. Very often, and fruitfully for applications, even the single degree of freedom (translational, vibrational or rotational) is not at the equilibrium condition because not fast enough process are present to guarantee the thermalization. It is not therefore possible to define the temperature as expression of the average energy and a full kinetic description is required to represent the system, taking into account the state-to-state nature of collision energy transfers, as we shall see in details in the next paragraphs.

The importance of non-equilibrium conditions in ionized gases is related to the selective production of reactive species (excited vibrational molecules, excited electronic state atoms, ions and radicals, photons, etc.). In particular, the low electron energy range (<10 eV) is responsible for rotational and vibrational excitations of molecules, that are precursors for the formation of hot atoms and negative ions by the dissociation channel, while electrons in middle energy range are responsible for the production of electronic excited and ionic species. The production rate of such species (f) is described by the reaction frequency (or rate) defined as the product of the reaction rate coefficient k_{if} and the density of the target specie (i):

$$\nu_{if} = k_{if} N_i = N_i \int \sigma_{if}(v) v f_p(v) dv. \tag{2}$$

The production rate heavily depends on the kinetic characteristic of the components, as the distribution function of the projectile $f_p(v)$, the state-selective cross section $\sigma_{if}(v)$, which reflects the quantum mechanical structure of the target. The target and final product species can be any single atomic/molecular ro-vibronic level whose population N_i can be orders of magnitude larger that the equilibrium one. Tailoring the non-equilibrium plasma to a particular application often means to adapt the working conditions such as to maximize the functional integral (2) for a specific class of processes. This concept embodies the importance of the non-equilibrium condition in ionized gases and its atomic/molecular basis. We shall provide in the next some examples that will clarify it.

To increase the degree of non-equilibrium in plasmas there are then two ways: operate at low pressure, to reduce energy transfer rates or, at high – typically atmospheric – pressure (ATP), provide fast pulsed energy input. It is customary in the past literature to classify NTP systems as low pressure – less than 10 Torr – systems, due to the fact that research efforts were almost exclusively devoted to technological devices operating at low pressure. Nowadays, after an increased interest in the last two decades into ATP discharges, it is well known that strong non-equilibrium conditions are achieved as well at high pressure, as a consequence of a ns scale pulsed nature of the applied electric field in micrometer discharge size.

3 Non-equilibrium in the electron distribution function (EDF)

As mentioned in previous Section 2, electrons play a crucial role in NTP. Their distribution function is defined by the interplay of a variety of plasma kinetics, transport and electrodynamic processes. In all systems, the energy is first transferred to electrons due to their high mobility, and then transmitted to all other plasma components by ionization, excitations, dissociation processes. For this reason the non-equilibrium in the electron sub-system can significantly influence transport quantities (drift velocity, diffusion coefficient, mobility, etc.) and plasma-chemical reaction rates and will be first described. A particular aspect of the non-equilibrium condition for electrons is related to non local kinetic regime: it consists of a complete de-correlation between plasma parameters and heating electromagnetic field space-time distributions. Such a condition occurs at sufficiently low gas pressures when the electron energy relaxation length is larger than

the discharge size and an electron collides with atoms and crosses the plasma practically without changes in its total energy. It allows the modification and tailoring of electron distribution function (EDF) according to specific purposes [1].

The electron degrees of freedom that can be out-of-equilibrium are the velocity components and then the translational energy. The fundamental quantity describing the electron behaviour in low temperature plasma is the electron velocity distribution function (EVDF) $f(\boldsymbol{r},\boldsymbol{v},t)$ that gives the probability distribution of particle velocity vectors $\boldsymbol{v}$ at any spatial position $\boldsymbol{r}$ and at any instant t:

$$dN(\boldsymbol{v}) = f(\boldsymbol{r},\boldsymbol{v},t)d^3\boldsymbol{r}d^3\boldsymbol{v}. \tag{3}$$

Its evolution is described by the Boltzmann equation (BE):

$$\frac{\partial f}{\partial t} + \boldsymbol{v}\cdot\nabla_{\boldsymbol{r}} f + \frac{\boldsymbol{F}}{m}\cdot\nabla_{\boldsymbol{v}} f = \left(\frac{\partial f}{\partial t}\right)_{coll} \tag{4}$$

where the force on an electron in electric field $\boldsymbol{E}$ and magnetic field $\boldsymbol{B}$ is given by the Lorentz force $\boldsymbol{F} = q(\boldsymbol{E} + \boldsymbol{v}\times\boldsymbol{B})$, while the term $(\partial f/\partial t)_{coll}$ accounts for the effects of collisions, and can take different forms on the basis of the peculiar interaction potential governing the encounter between the electron and the collision partner.

Under equilibrium condition, i.e. after a sufficient time interval (thermalization time) necessary to exchange energy with the electric field and with the other plasma/gas particles, the solution of BE is homogeneous and stationary and takes the form of Maxwellian velocity distribution function at a temperature T_e:

$$f^{Maxw}(\boldsymbol{v}) = \left(\frac{m}{2\pi kT_e}\right)^{3/2}\exp\left(-\frac{m|\boldsymbol{v}|^2}{2kT_e}\right) \tag{5}$$

whose one-dimensional component is:

$$f_{1D}^{Maxw}(v_x) = \left(\frac{m}{2\pi kT_e}\right)^{1/2}\exp\left(-\frac{mv_x^2}{2kT_e}\right). \tag{6}$$

Due to its isotropy, the EVDF can also be expressed in term of speed distribution

$$f_s^{Maxw}(v) = \left(\frac{m}{2\pi kT_e}\right)^{3/2} 4\pi v^2\exp\left(-\frac{mv^2}{2kT_e}\right). \tag{7}$$

The corresponding electron energy distribution function (EEDF) is represented by the Maxwell-Boltzmann expression

$$f^{MB}(\varepsilon) = 2\sqrt{\frac{\varepsilon}{\pi(kT_e)^3}}\exp\left(-\frac{\varepsilon}{kT_e}\right)[\mathrm{eV}^{-1}]. \tag{8}$$

Quite often, the so called electron energy probability function (EEPF) is used; it is defined as the EEDF divided by the square root of the energy ($f_p(\varepsilon) = f(\varepsilon)/\varepsilon^{1/2}[\mathrm{eV}^{-3/2}]$) and for a Maxwell-Boltzmann this gives a single straight line on a semi-log plot. It allows to quickly visualize the electron temperature as inversely proportional to the slope of the EEPF.

Among the different reasons leading to non Maxwell-Boltzmann EEDF in weakly collisional plasma there are:

1. the rapid spatial and/or temporal variation of the electrostatic or electromagnetic fields;
2. the presence of boundaries (electrodes, walls or catalytic surfaces);
3. the presence of high anisotropy;
4. inelastic and super-elastic collisions, where the electron kinetic energy is exchanged with internal degrees of freedom of atoms/molecules.

Three families of non-Maxwellian distributions are most commonly found in laboratory and space plasmas: Druyvesteyn, bi-Maxwellian and Lorentzian k-law distributions.

The exponential-parabolic Druyvesteyn distribution:

$$f_{1D}^{Druy}(v) = 18A_D\left(\frac{m}{6\sqrt{2}\pi k_BT_e}\right)^{3/2} \times\exp\left[-A_D\left(\frac{mv^2}{2k_BT_e}\right)^2\right] \tag{9}$$

where $A_D = \frac{[\Gamma(1/4)]^4}{72\pi^2} \approx 0.243$ and $\Gamma(x)$ is the Gamma function, is characterized by a larger middle-energy electron population and it decreases with energy much faster than the Maxwellian one for the same mean energy.

The electron distribution function in non-equilibrium discharges in noble Ramsauer gases is usually close to the Druyvensteyn distribution if the ionization degree is not as high as to make electron-electron collisions contribute to thermalization. For the same mean energy, an admixture of molecular gas (addition of inelastic vibrational excitation collisions comparable to elastic collisions), or a larger ionization degree (electron-electron collisions) tend to impart the Maxwellian character to the distribution function [2]. It is useful to parametrize the Druyvensteyn vs. Maxwellian behavior introducing the generalized EEPF:

$$f_p^N(\varepsilon) = c_1\exp(-c_2\varepsilon^N) \tag{10}$$

with $N = 1$ for Maxwellian and $N = 2$ for Druyvensteyn.

The bi-Maxwellian distribution is characterized by the combination of two Maxwellian populations with different temperatures T_H and T_C.

Finally, in the solar wind and in the planetary magnetospheres, the distributions have a suprathermal power-law tail at high energies [3], which has been well represented by the so called generalized Lorentzian power-law κ-distribution:

$$f_{1D}^{\kappa}(v) = \left(\frac{1}{\pi\kappa v_0^2}\right)^{3/2}\frac{\Gamma(\kappa+1)}{\Gamma(\kappa-1/2)}\left(1+\frac{v^2}{\kappa v_0^2}\right)^{-\kappa-1} \tag{11}$$

where the spectral index $\kappa > 1$ accounts for the deviation from the Maxwellian distribution: $f_\kappa \to f_{Maxw}$ as $\kappa\to\infty$. The second parameter v_0 allows to define the average energy and then an equivalent temperature $E_0 = mv_0^2/2 = [(2k-3)/2k)]k_BT_e$, for $k > 3/2$. On this basis, it was also shown that, in a κ-distributed plasma,

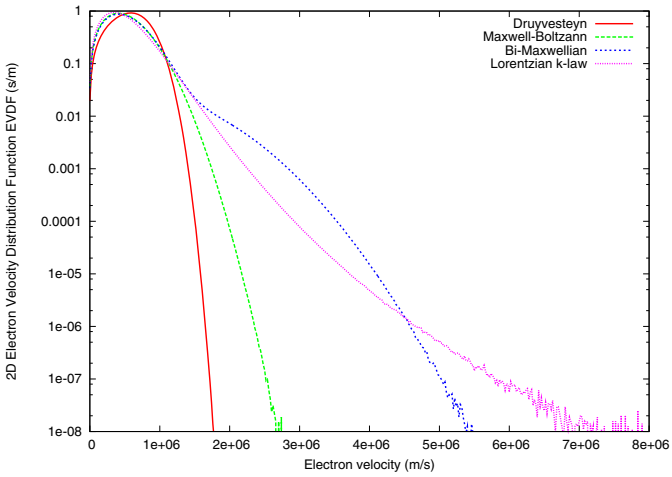

Fig. 1. The most common electron speed distribution function in plasmas: Druyvensteyn, Maxwellian and bi-Maxwellian and Lorentzian k-law distributions.

the Debye length is smaller than in a Maxwellian plasma: $\lambda_\kappa = \lambda_{Maxw}(2\kappa - 3)/(2\kappa - 1)$. The κ-distribution possesses a high-energy tail, with a power law dependence $f_\kappa \propto E^{-\kappa-1}$ for $E \gg \kappa E_0$.

In Figure 1 the electron speed distributions of the most common cases are reported for comparison.

In the following we shall analyze some non-equilibrium electron distributions obtained in various case studies over the past decade.

3.1 Electrons in the loss cone: plasma-wall transition regions

At plasma-wall transition region the bulk potential falls sharply, providing a high electric field, acceleration of ions, and deceleration of electrons. The basic one-dimensional equation governing the DC sheath potential $\Delta\phi_{sh}$ in the direction perpendicular to the wall is often obtained with a fluid treatment: from the Poisson equation, energy conservation for the ions, and the Boltzmann distribution for electrons. Balancing the ion and electron fluxes to the wall leads to the expression for the potential drop across the sheath:

$$\Delta\phi_{sh} = \frac{kT}{e} \ln\left(\sqrt{\frac{M}{2\pi m}}\right). \tag{12}$$

However, the fluid approach and as a consequence equation (12) is not appropriate in many real cases. The effect of the sheath on EVDF consists of a depletion of the high-energy tail (loss cone in the velocity space): electrons with enough energy to overcome the sheath potential (12) $w_x > e\Delta\phi_{sh}$ escape from the plasma to the walls, where they are lost (x here represents the direction perpendicular to the wall). In addition, the characteristic size of the discharge L is often smaller than the electron mean free path $\lambda_{e,coll}$ and the EVDF resulting from the electron-sheath interaction is not able to relax towards a Maxwellian. The non-Maxwellian character of the EVDF strongly affects

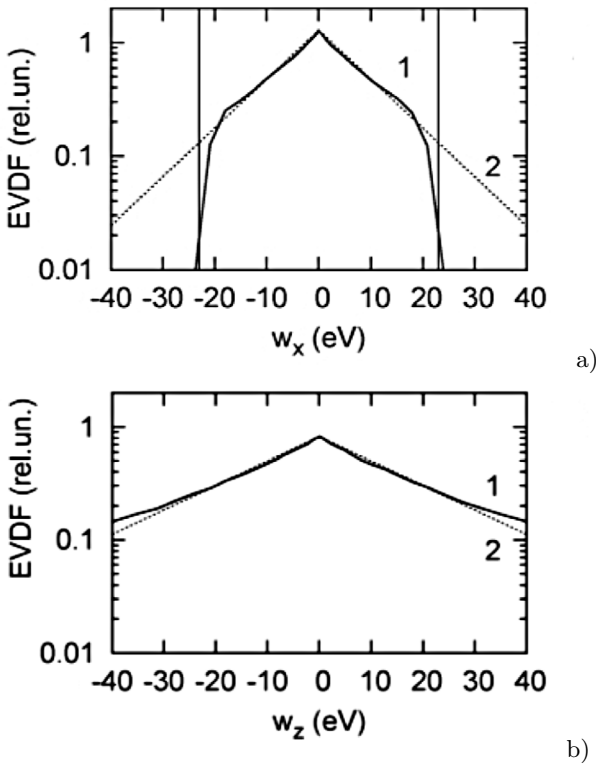

Fig. 2. EVDF over (a) normal w_x and (b) parallel w_z to the wall kinetic energy (the sign marks the velocity direction). On both figures, curve 1 is the result of kinetic simulation and curve 2 is the fitting Maxwellian ($T_x = 10.1$ eV and $T_z = 20.1$ eV). In (a) the two symmetric vertical lines mark the confinement threshold energy $w_x = e\Delta\phi_{sh}$ [5]. ©2006 IEEE.

the effective electron temperature, the electron flux to the wall and as a consequence the sheath drop itself [4].

As an example, in Figure 2, two components of EVDFs, normal $f_{LC}(w_x)$ and parallel $f_{Maxw}(w_z)$ to the wall, have been reported as results of kinetic numerical models [5]. The EVDF normal to the wall appears to be close to a Maxwellian only for electrons trapped in the potential well, i.e. with energy small compared with the wall potential (confinement threshold) $w_x < e\Delta\phi_{sh}$. For higher energies the electron population is strongly depleted, while the EVDF parallel to the wall keeps a Maxwellian behaviour. It has been shown that the EVDF in the loss cone is smaller by a factor of $\mathcal{O}(L/\lambda_{e,coll})$ compared with the EVDF outside the loss cone [4]. Under such conditions the effective temperature ($T_{eff} = \frac{m}{k_B}\int_{\infty}^{-\infty} f_{LC}(v)v^2dv$) results smaller than that corresponding to the unperturbed Maxwellian electron population by the factor:

$$\frac{T_{LC}}{T_{Maxw}} \approx \frac{e\Delta\phi_{sh}}{e\Delta\phi_{sh} + kT_{Maxw}}. \tag{13}$$

As a consequence, the electron flux to the wall in the large electron mean free path limit $\lambda_{e,coll} \gg L$ is reduced by a factor of $\mathcal{O}(L/\lambda_{e,coll})$ compared with the calculation assuming an EVDF with a filled loss cone

and the potential drop in the sheath reads:

$$\Delta\phi_{sh} = \frac{kT_{Maxw}}{e} \ln\left(\frac{L}{\lambda_{e,coll}}\sqrt{\frac{T_{Maxw}}{T_{LC}}}\sqrt{\frac{M}{2\pi m}}\right) \quad (14)$$

leading to a sheath potential drop about five times smaller than the fluid-Maxwellian prediction equation (12). Although the sheath potential drop in the non-Maxwellian loss cone case is much smaller than those in Maxwellian cases, the plasma-wall interaction results much weaker since the loss cone EEDF is depleted at high energies.

3.2 Non classical sheath with strong secondary electron emission

The presence of electron-emitting surface is almost ubiquitous in many laboratory and space plasmas (e.g., capacitively coupled plasmas, divertor plasmas, dc hollow cathode discharges, dc magnetrons, electric thrusters, dusty plasmas, the Moon, etc.). The case of electron emission induced by primary electrons (secondary electron emission SEE,) rather than thermionic or photon-induced emissions, is particularly interesting because it is able to drive non-classical and unstable sheath regimes [6,7]. The effect of secondaries emitted from a surface has induced many macroscopic behaviour in different plasma-based devices (near-wall conductivity in Hall-effect thruster (HET) [8]) and is the basis of diagnostic techniques, such as emissive probe [9].

The sheath with SEE has been treated by fluid model in the seminal work of Hobbs and Wesson [10], who derived the expression for the potential sheath drop

$$\Delta\phi_{sh} = \frac{kT_e}{e} \ln\left[(1-\Gamma)\sqrt{\frac{M}{2\pi m}}\right] \quad (15)$$

where Γ is the ratio of electron emitted flux per plasma electron influx. The potential drop reduces up to value of $\Delta\phi_{sh} \approx kT_e/e$. Kinetic models [11] have showed that the classical Debye layer disappears when $\Gamma > \Gamma_{SCL} \approx 1$–$8.3\sqrt{(m/M)}$ and transforms into a non-monotonic double layer structure (space charge limited SCL regime). A potential well and virtual cathode forms close to the wall which traps a fraction of secondary electrons in order to ensure the zero current condition there, but still keeping a positive sheath potential drop (the potential at the sheath edge is larger than the wall value). In case of higher Γ the sheath can be completely reversed leading to a different presheath structure and violation of the Bohm's criterion at the sheath edge [12], and it can even lose its static character giving rise to high-frequency fluctuations (∼20 MHz). This plasma sheath instability is due to the negative differential resistance branch in the I-V trace of the surface contacting the plasma [13–15]. The sheath current boundary conditions lead to the positive feedback that destabilizes the ion sound waves [16].

Under certain conditions, electrons emitted from one surface can be accelerated and induce a strong emission from the opposite wall leading to a self-amplification of secondary emission and to beam-plasma or two-stream instability [17,18]; in Figure 3 the typical bump-on-tail shape of EVDF in HET has been reported as result of kinetic model [18]; the bump represents the contribution of secondaries and if the Penrose criterion is reached, the population can lead to instability in the bulk plasma.

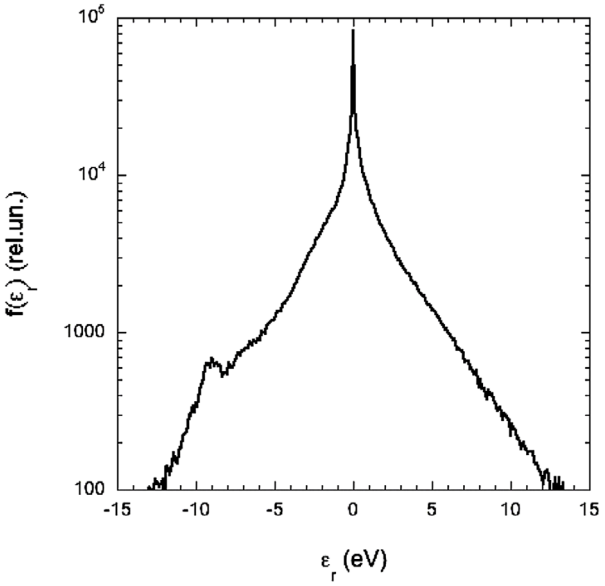

Fig. 3. Radial kinetic electron distribution function computed in HET simulation [18] due to the strong emission of secondaries from the outer wall and directed in the bulk plasma (negative radial energy value).

3.3 Anisotropy in E × B devices

Electron confinement with magnetic field is often used in laboratory plasmas for different reasons. It reduces plasma diffusion to the wall, thus increasing plasma uniformity and its density at the same discharge power. Non-uniform magnetic field confines fast electrons better than cold ones, thus performing a filter between hot and cold electrons [19]. This feature is widely used in negative hydrogen ion sources to reduce negative ion destruction by electron detachment and increase negative ion to electron extracted current ratio [20]. Finally, electron magnetic confinement is often used in $E \times B$ configuration (Hall-effect thruster HET, magnetron and Penning discharges) in order to increase ionization efficiency and create a strong impedance with a virtual cathode to accelerate the generated ions.

In $E \times B$ low pressure discharges electron distribution function is not Maxwellian. This is due to the fact that the mean free path between collisions is greater than both the Larmor radius and the characteristic dimensions of the discharge. In addition, due to the $E \times B$ drift, $v_{E\times B}$, a strong anisotropy between the different components is present. The problem can be parameterized in terms of the $E \times B$ drift normalized to the thermal velocity, w, and the Hall parameter β (ratio between collision and cyclotron

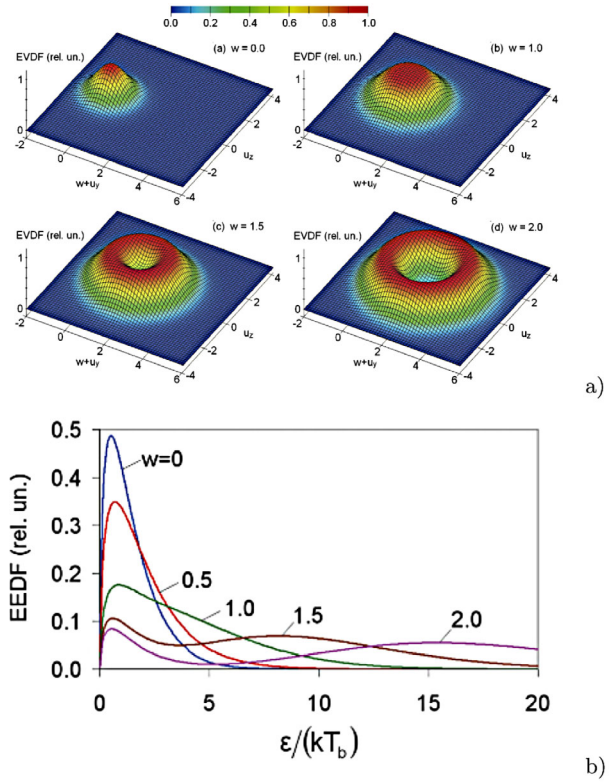

Fig. 4. (a) EVDF over y and z velocity components (normalized to thermal velocity) and (b) EEDF at several values of the dimensionless drift velocity w for $\beta \to 0$ [21]. ©2012 American Institute of Physics.

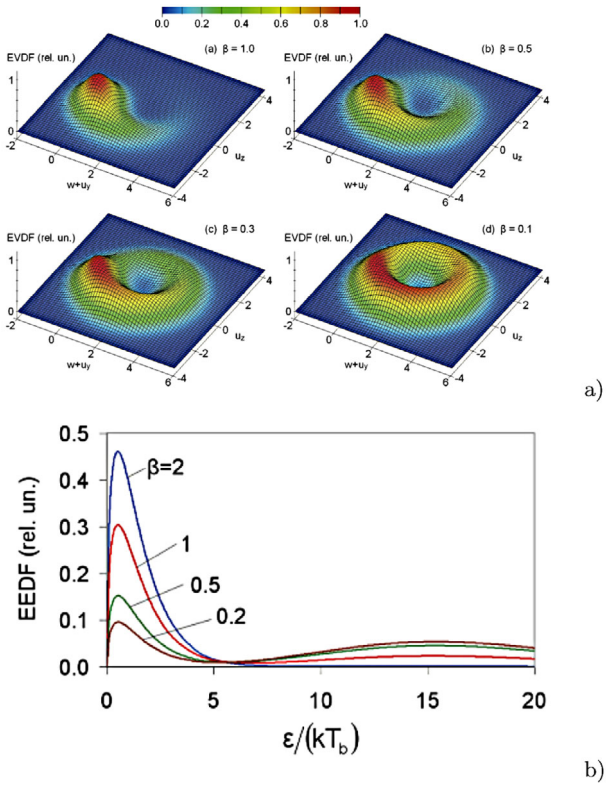

Fig. 5. (a) EVDF over y and z velocity components (normalized to thermal velocity) and (b) EEDF at several values of Hall parameter β for $w = 2$ [21]. ©2012 American Institute of Physics.

frequency). Figure 4a shows EVDF in two dimensions, both orthogonal to B field (y along $E \times B$ direction and z along E) for several values of w at fixed β [21]. With the increase of w, the deviation from the equilibrium function increases, and EVDF becomes crater-shaped. The crater walls show the location of the electrons on the cyclotron rotation trochoids. The corresponding EEDFs are reported in Figure 4b. As w increases, the EEDF acquires a second peak, typical of a gyro-motion [22]. Figure 5a shows EVDF at different β for $w = 2$. With decreasing collision frequency (or increasing magnetic field) the distribution deviates more and more from the Maxwell shape (high β): smearing of the EVDF occurs along the circle corresponding to the cyclotron rotation of the electrons in the velocity space. The corresponding EEDFs are shown in Figure 5b. Note that with the increase of collision frequency, the positive derivative near the second peak decreases.

The deviation from Maxwellian distribution has an important consequence on the so called anomalous electron cross-field transport: the deviation directly influences collisional rate [22], it changes the electron flux to the wall and the resulting secondary electron emission (near-wall conductivity [8]). In addition, it strongly interacts with electron cyclotron drift instability (ECDI) [23,24], considered as the most likely source of the azimuthal fluctuation along the $E \times B$ direction; the proof of this interaction relies on the appearance of a plateau, corresponding to the saturation of the first unstable mode ($k_y v_{E\times B} = 2\pi\omega_{ce}$), and by an heating in the electron distribution function [25,26].

3.4 Bi-Maxwellian EEDF in RF-capacitive coupled discharge

Capacitively coupled radio frequency (CCRF) discharges are particularly used for etching, sputtering and deposition of thin films. Older studies have shown that a transition in the electron heating mechanism is driven by lowering the gas pressure: from ohmic heating due to collisions of electrons with neutrals to stochastic Fermi heating due to momentum transfer from the oscillating sheath. The most relevant kinetic effect of the stochastic heating is the change of the EEDF [27]: at higher pressure the distribution becomes dome-shaped Druyvestein-like, with a distinct reduction in the number of higher-energy electrons, while at low pressure a high-energy tail (characterized by a temperature $T_e > 5$ eV) is superimposed on a cooler bulk ($T_e < 5$ eV) leading to a bi-Maxwellian shape. More recently, a renewed interest in CCRF discharges has enabled the driving of kinetic studies that have provided a number of interesting results on the electron heating mechanism; in particular, the following effects deserve a quote:

1. the possibility to modulate the confinement of energetic multiple electron beams generated at one

electrode during the sheath expansion phase by the driving frequency [28]; the modulation works on the interaction between the beam and the sheath moving in the opposite direction, allowing to control the shape of the EEPF by adjusting the frequency. This is important for applications, since it might allow to customize the plasma chemistry in more complex gas mixtures;
2. the interplay between high energy beam electrons and low energy bulk electrons as the origin of the generation of harmonics in the discharge current [29];
3. a critical kinetic revision based on the works of Kaganovich et al. [30] and Lafleur and Chabert [31] shows that the true collisionless/stochastic heating contributes only for a small amount to the electron heating and that collisions are needed to generate the non-ohmic heating component which in fact appears as the result of non-local collisional heating.

Similar relation between anomalous heating and non equilibrium EEDF can also be found in different low-pressure plasma discharges, such as dc glow [1] and inductively coupled plasmas (ICP) [1]. In addition, the low energy peak detected in CCRF is also common to stratified DC plasmas and ICP at low gas pressure [32]. It is a feature of non-local electron kinetics when low energy electrons are trapped and cannot reach the area of the heating field localization.

3.5 Electrons in laser-induced photo-detachement

Laser photo-detachment has been used as a diagnostic tool for negative ion density and temperature measurements [33]. The photo-detachment diagnostic method consists of producing a negative ion free region via laser photo-detachment $h\nu + H^- \rightarrow H + e$ within an electronegative plasma bulk. The pulsed laser (duration of a few ns) fluence is chosen such as to ensure a total destruction of negative ions within the illuminated region, without exciting atoms or producing photoionization. An electrostatic probe is located within the illuminated region to track the electron density evolution. The negative ion density can be determined from the increase of electron density within the illuminated region. The method is based on the assumptions that background electrons remain unperturbed Maxwellian during the response of the plasma to the laser pulse and that photodetached electrons instantly thermalize with background electrons. Kinetic models [34,35] have shown that the background electron population is heated and the distribution function deviates from a Maxwellian due to the presence of a potential barrier on the border of the electropositive channel; the photo-detached electrons have a different temperature and distribution relative to the background group. Both groups are strongly perturbed by the presence of the double layer barrier. Figure 6a shows the background electron radial velocity distribution function obtained inside the laser-spot region at different times, using a laser photon energy of 2.33 eV. At $t = 1$ ns, background electrons have a Maxwellian distribution function with a temperature of $T_{bg,e} = 1$ eV.

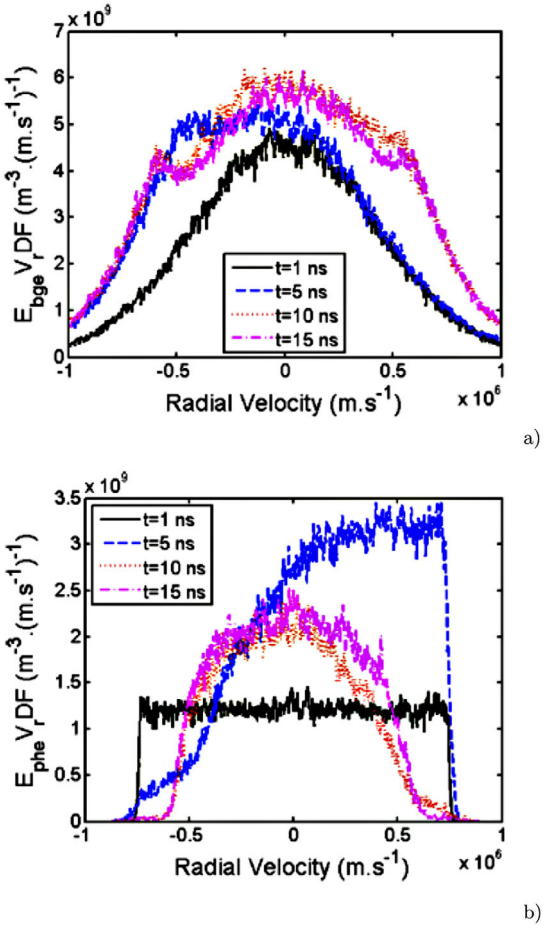

Fig. 6. (a) Background and (b) photo-detached electron radial velocity distribution function at different times after the laser photodetachment [35]. ©2015 AIP Publishing LLC.

At $t = 5$ ns, background EVDF becomes asymmetric with a positive skewness (negative average radial velocity). This is due to the flux of background electrons entering the electropositive channel. At t =10 ns and $t = 15$ ns, the background EVDF have tails peaking at $\pm v_{peak}$. Figure 6b shows the corresponding photo-detached electron radial velocity distribution function. The water-bag shape at $t = 1$ ns evolves towards a smooth distribution function, passing through a strong asymmetrical distribution ($t = 5$ ns). This asymmetry is the sign of the potential barrier that confines the photo-detached electrons inside the electropositive channel. The non-Maxwellian character of the electron population leads to an increase in the electron current collected by the probe and then to an erroneous determination of the negative ion density.

3.6 Role of electron-atom/molecule cross sections shape

This paragraph deals with the effects of collisions on the deviation of electron distribution function from Maxwellian behavior. A strong dependence of cross sections on the electron kinetic energy can have a deep

influence on the EEDF, especially at low external energy input. In an electrical discharge this corresponds to low applied electric field or, ultimately, to post-discharge (afterglow) conditions, where the electric field is zero.

A striking example is the effect of electron attachment to electronegative molecules, whose cross section is effective only at low (< 2–3 eV) electron energy (see for example Fig. 21 in Sect. 5.3). Attachment can then severely deplete the low energy part of the EEDF if this is not refilled by other processes like elastic or Coulomb collisions.

The EEDF is also strongly affected by inelastic collisions with sharp cross sections characterized by a threshold energy, a peak region and a decrease at high energy. A good example is represented by N_2 vibrational excitation reported in Figure 15 in Section 5.1.1. In discharges with low electric field, energy transfer to nitrogen molecular vibration sharply depletes the EEDF roughly in the 2–6 eV energy range.

Inelastic electron collisions have the corresponding reverse process. Both processes can be schematized as:

$$e(\varepsilon + \Delta\varepsilon) + M \rightleftarrows e(\varepsilon) + M^*, \qquad (16)$$

in which M^* is an atomic electronic state or any molecular ro-vibronic state. It is customary to call the reverse process superelastic, or second kind, collision. It can play a major role in creating structures in EEDF, through the release of a well defined high energy quantum $\Delta\varepsilon$ to the electron ensemble. A recent survey on this topic can be found in Chapter 5 of [36]. Superelastic collisions are effective whenever a high concentration of excited states at low electron temperatures is realized. Such conditions are usually found in afterglow plasmas, where the electron energy rapidly decreases while the population of excited species, especially metastable states, survives for much longer time, or in optically thick plasmas, where photon re-absorption tends to increase the concentration of excited states. At high ionization degrees, electron-electron (Coulomb) collisions, that are more effective at low electron energy, tend to smooth the selective energy input of superelastic collisions. As an up-to-date example we mention the recent study of a nanosecond high-voltage dielectric barrier discharge (DBD) in CO_2 at atmospheric pressure [37]. In Figure 7 it is reported the electron energy distribution function at different vibrational temperatures (symmetric T_v' and asymmetric T_v normal modes) in the post-discharge regime. We can see that superelastic collisions from the excited electronic level $CO_2(e_2)$ forms a source of electrons at the threshold energy for the excitation process, i.e. 10.5 eV, which is transformed in a plateau by elastic and inelastic collisions, including Coulomb collisions. The plateau length strongly decreases with the increase of vibrational temperatures.

Finally, we mention that even elastic, momentum transfer, scattering can, in particular conditions, induce EEDF deviation from equilibrium. The combination of energy dependence of the cross section with finite plasma size can result in an energy selective loss of electron population. A description of such processes, that are typical of swarm experiments, can be found in [38] and references therein.

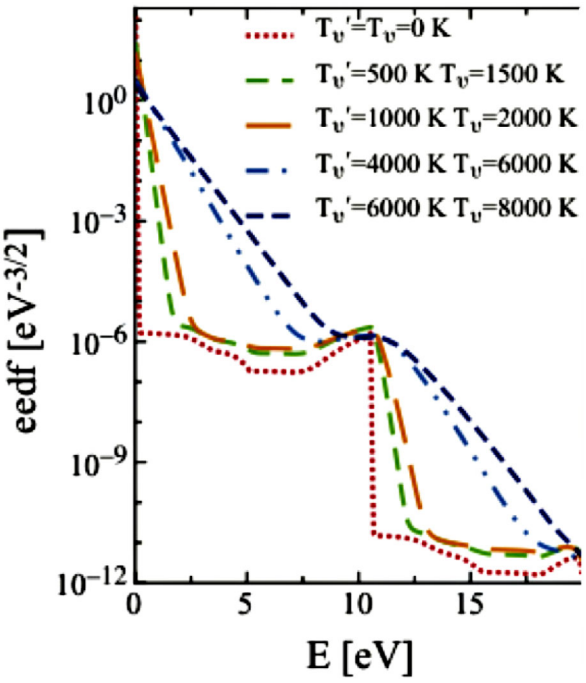

Fig. 7. Electron energy probability distribution function at $E/N = 30$ Td and ionization degree $\chi_e = 10^{-3}$ for different selected values of CO_2 symmetric T_v' and asymmetric T_v normal modes vibrational temperatures [37]. ©2015 IOP Publishing.

Table 1. Dust charge and surface potential and shielding length computed for the various distributions using PIC model.

	Q_d/e	ϕ_d	Δ_{sh}
Druyvesteyn	−22284	−2.33 V	$\approx 1.4\,\lambda_D$
Maxwell-Boltzmann	−30619	−2.86 V	$\approx 1.4\,\lambda_D$
Bi-Maxwellian	−42460	−4.06 V	$\approx 1.2\,\lambda_D$
Lorentzianκ-Law	−59335	−2.75 V	$\approx 0.5\,\lambda_D$

3.7 Electron energy distribution function in dusty plasmas

Plasmas with nano- and micrometer-sized particles are of great interest in different fields including astrophysics [39], soft matter [40], fusion [41] and processing plasmas [42]. Such particles acquire a negative charge Q_d and potential ϕ_d whose values strongly depend on the actual form of electron distribution function through the zero current condition at the particle surface. In Table 1, the charge and surface potential of the dust under the different electron distribution functions have been reported using the same effective temperature $T_e = 1$ eV for different electron distributions (for the *bi-Maxw* $T_C = 1$ eV, $T_H = 10$ eV and $n_H = 5\%$). These results have been obtained by means of a self-consistent kinetic model using Argon plasma with density $n_p = 2 \times 10^{16}$ m^{-3} and ion and neutral temperature $T_i = T_n = 0.025$ eV. Differences of the order of 25% and 40% are found in the dust charge and surface potential, respectively. As expected, the distributions with the most overpopulated high-energy tail (Lorentzian κ-law) induce the largest negative dust charge. On the contrary,

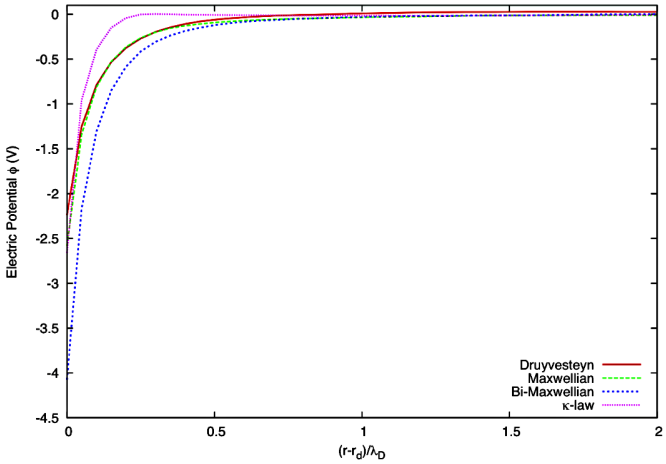

Fig. 8. Radial profile of the electric potential around the dust for the different electron distributions.

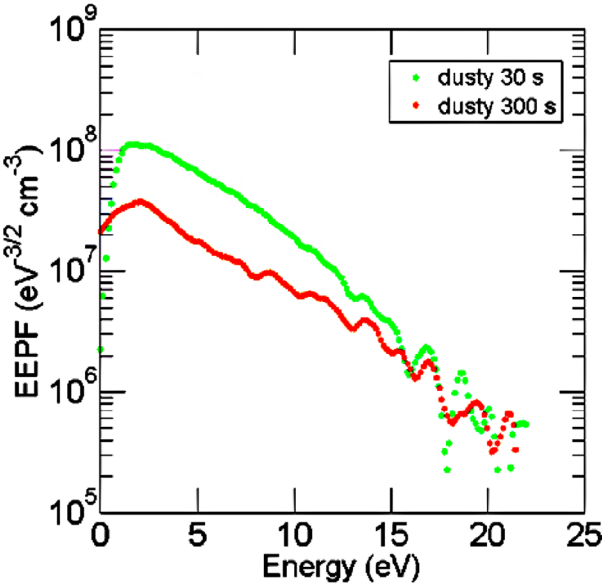

Fig. 9. EEPF 30 s and 300 s after initiation in a dusty argon-silane plasma maintained at 80 mtorr [43]. ©2015 IOP Publishing Ltd.

κ-distribution does not induce the deepest dust surface potential. The reason has to be found in the structure of the electric potential around the dust (see Fig. 8): the κ-law distribution induces a thinner sheath (smaller screening length Δ_{sh} as already observed in Sect. 3). This means that there are less electrons to be repelled by the dust charge and this leads to a smaller dust surface potential.

As well as the different EEDF shapes affect the dust particle properties immersed in plasmas, the presence of the particles affects the effective shape of electron distributions. Recent works [43,44] have shown that the presence and growth of dust particles change the EEDF shape from Druyvensteyn towards Maxwellian. Figure 9 shows EEPF in RF argon-silane plasma from Langmuir probe measurements at two different times during the dust particle growth, demonstrating the significant loss of mid-energy range (4–10 eV) electrons due to electron-particle collisions. Differently from the loss-cone case (Sect. 3.1), here the high energy electrons do not hit the dust surface due to the centrifugal barrier. The fitting gives $n = 1.9$ after 30 s and $n = 1.3$ at $t = 300$ s (see Eq. (10)), showing that the 30 s dusty EEPF is more Druyvesteyn-like and the 300 s EEPF is more Maxwellian-like. As nanoparticles nucleate and grow in plasma, the electron temperatures rises from ≈3.3 eV for the dust-free plasma up to ≈4.5 eV due to the drop in the low energy electron population. This increase in the electron temperature is required to maintain a relatively constant ionization rate as the electron density decreases because of attachment losses to the dust particle surfaces.

3.8 Electron energy distribution function in atmospheric pressure microdischarges

Low-temperature atmospheric-pressure microplasmas constitute a new realm in plasma physics with potential impact in aerospace, biomedical and environmental applications [45,46]. The reduced size of a microdischarge provides a large surface-to-volume ratio, makes the energy relaxation length comparable to the discharge gap (non local effects) and favours large electric fields and steep space gradients. These characteristics, despite the high collisionality, enable a departure from thermodynamic equilibrium with strong impact on the properties and reactivity of such devices [47]. It has been shown by means of kinetic models [48] that the EEPF in atmospheric-pressure microdischarge present a two-energy group distribution at smaller gap spacing d (as in low pressure discharges, Sect. 3.4) and a three-energy group distribution at larger gaps (see Fig. 10b). The relative population of electrons in different energy regions can differ by orders of magnitude from the values corresponding to Maxwellian leading to an effective electron temperature ten times smaller than obtained by a fluid description. The same characteristic has been found in RF atmospheric-pressure microdischarges, for which again the electron energy relaxation time is significantly shorter than the RF period leading to a strong time modulation of electron energy distribution. The three electron groups can be identified as follows: (1) low-energy electrons ($\varepsilon < 2$ eV, limit representing the minimum sheath drop during the sheath collapse) trapped by the ambipolar potential and not affected by collisional and/or collisionless heating; (2) middle-energy electrons (2 eV $< \varepsilon <$ 20 eV, where 20 eV corresponds to the excitation threshold, here He) formed in the sheath by high-energy electrons and that do not last for the whole RF cycle because lost to the electrodes during the sheath collapse; as in low-pressure discharges, the knee in the EEPF is due to the faster energy relaxation of electrons in the inelastic energy range; (3) high-energy electrons ($\varepsilon >$ 20 eV) representing ion-induced secondaries produced at the anode (the discharge is sustained in the so-called γ mode), accelerated in the sheath and that lose their energy in the plasma region. In Figure 10

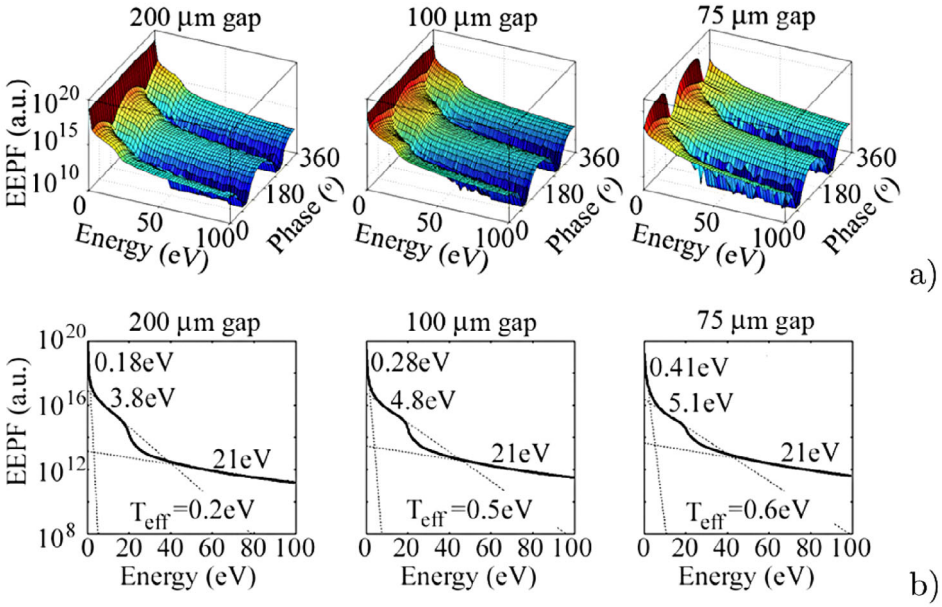

Fig. 10. Time evolution of the EEPF in three He microplasmas at atmospheric pressure driven at 1 A/cm^2. (a) EEPF accounting for electrons in the whole gap. (b) Space and time-averaged EEPF [49]. ©2007 The American Physical Society.

the EEPFs in He microplasmas at atmospheric pressure driven at 13.56 MHz – 1 A/cm^2 with different electrode gaps have been reported as (a) time evolution in the whole gap and (b) space- and time-averaged [49].

The same EEDF structure and underlying principles are found in dielectric barrier discharges (DBD). Here, an additional knee at lower energy is observed and the low-energy electrons have a higher temperature and are less abundant than DC and RF microdischarges [45]. These differences are due to the presence of a temporary anode on dielectric surface and to the shorter duration of the discharge compared to the energy relaxation time.

3.9 K-law distribution in space plasmas

Most astrophysical and space plasmas are observed to have non-Maxwellian high-energy tails [3]. κ-distributions with $2 < \kappa < 6$ have been found to fit the observations and satellite data in the solar wind, Earth's and Mercury's magnetosphere, the plasmasheet of different planets, the magnetosheath, the radiation belts [3].

Among the various mechanisms proposed to explain the origin of such a suprathermal tail in space plasmas there is the behaviour of Coulomb cross section ($\sigma(\varepsilon) \propto \varepsilon^{-2}$): the fast particles are nearly collisionless in space plasmas, they are easily accelerated and tend to produce non-equilibrium velocity-distribution functions with suprathermal tails decreasing as a power law of the velocity.

The presence of a high-energy tail component in a κ-distribution considerably changes the rate of resonant energy transfer between particles and plasma waves so that the dispersion relation, the conditions for Landau damping of Langmuir and ion acoustic waves and plasma instabilities can be substantially different for Maxwellian and κ

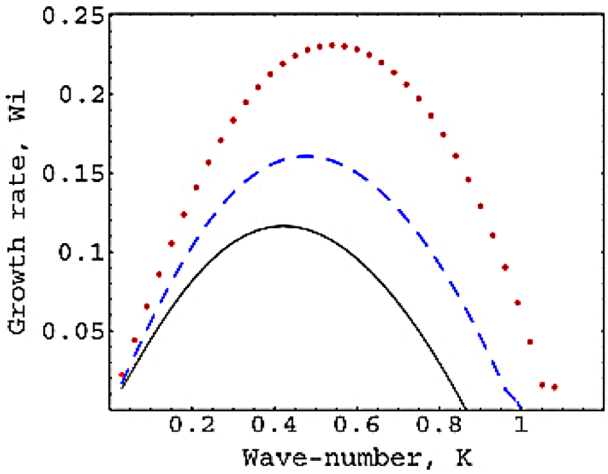

Fig. 11. Dependence of growth rates of two-stream instability, for the spectral index $\kappa = 2$ (the red dotted lines), 4 (blue dashed lines), and for Maxwellian $\kappa \to \infty$ (black solid lines) plasmas. Here the parameters are typical for solar-wind conditions: plasma temperature $T_e = 170$ eV and symmetric counter-streams with the same temperature, and the bulk velocity $v_0 = 0.1c$ (where c is the speed of light). The coordinates are scaled as $Wi = \omega_i/\omega_{pe}$ and $K = kv_0/\omega_{pe}$ [3]. ©2010 Springer.

distributions [50]. Suprathermal populations enhance the electrostatic instability leading to an increse of its growth rate for lower κ (see Fig. 11). The suprathermal particles also increase the escape flux in planetary and stellar wind and can explain the acceleration of the fast solar wind. For low values of κ, the heat flux changes sign so that heat can flow from cold to hot. Finally, as observed in Section 3.7, dust charge and surface potential under electron

κ-distribution has shown important differences from dust characteristics in Maxwellian electrons [51].

4 Non-equilibrium in the ion energy distribution function (IEDF)

Since ions are heavy particles, the faster collision energy transfer to the neutral gas results in a Maxwellian ion energy distribution function, with a temperature close to neutral gas temperature. Nevertheless, there are different reasons why the ion energy distribution can be far from MB and the actual distribution has an important impact on the general macroscopic behaviour. In the following sections we shall examine some recent examples.

4.1 IEDF in electric thruster plume

The full characterization of the ion beam in the plume emitted by electric thrusters [52], in particular at angles beyond the main beam divergence, is important for possible damaging effect caused by exhaust ions impinging upon spacecraft surfaces. The IEDF is also directly related to the thruster performance through the energy dispersion η_{dE} and the divergence $\eta_{d\theta}$ efficiencies of the ion beam

$$\eta_{dE} = \frac{\langle v_i \rangle^2}{\langle v_i^2 \rangle} \tag{17}$$

$$\eta_{d\theta} = \langle \cos\theta_i \rangle^2 \tag{18}$$

where the symbol $\langle\rangle$ represents the average over the ion population in the plume. Moreover, from ion distribution function moments, the time evolution of the electric field profile, the overlap between ionization and acceleration layers inside the discharge channel and the off-axis cathode location effect can be deduced [53,54].

The actual shape of IEDF in electric thruster plumes is not only related to the acceleration field phenomena (predator-prey and ion transit time oscillations), but it is also directly related to collisional phenomena occurring in the plume. In fact, even though the population is dominated by highly energetic ions accelerated directly by the applied electric field, sources of secondary ions generated by elastic (momentum transfer MT) and charge exchange (CX) collisions between main-beam ions and neutral unionized gas propellant are present, representing about 15% of the total population. Ions in this second population, due to their low energy, are expelled from the main plume by radial forces, and thus dominate at large plume angles ($\psi > 70$ deg, being ψ the angle off axis).

Figure 12 shows ion-energy spectra measured at different plume angles with respect to the thruster axis [55] using a collimated retarding potential analyzer (RPA). Apart from the angle-independent high-energy peak at the thruster discharge voltage associated with the main beam, two additional peaks are evident: the CX ions peak at low energy (about 10 eV) and a variable energy peak. The energy depends on the angle nearly as $\cos^2\psi$, providing

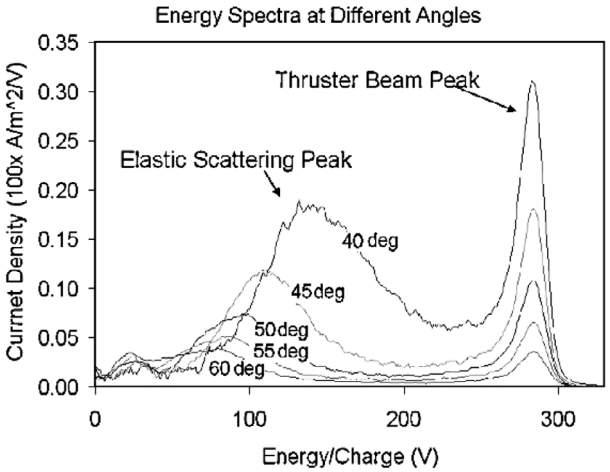

Fig. 12. Collimated RPA measurements at various angles with respect to thruster axis of symmetry [55]. ©2004 American Institute of Aeronautics and Astronautics, Inc.

strong evidence that these ions result from elastic scattering of main-beam ions by neutrals. In addition, for high voltage discharge, a high-energy tail with energy larger than the discharge voltage has also been detected [53,56]. The origin of these super-high-energy ions result from two different mechanisms: CX and momentum transfer processes in collision events that involve multiply charged ion species and ion surfing on ion transit time axial wave.

4.2 IEDF for nanoparticle growth in plasma

The importance of ion-atom resonant charge exchange CX reaction is also often associated to the increment of ion current collection by a negatively biased electrical probe at intermediate pressure range [57]. An ion-atom CX collision breaks the ion angular motion around the probe and leaves it with insufficient total energy to escape from the potential well surrounding the probe (orbital motion destruction). This mechanism induces an ion current enhancement towards the probe at intermediate pressure. In the opposite case of a very large number of collisions, the ion current to the probe is limited by diffusion and drift to the probe. The current then decreases with increasing pressure. The same mechanism can explain why the growth of crystalline nanoparticles is favoured at intermediate pressure regime [58,59]. In fact, low-energy ions activate ion-surface processes that cause surface atom displacements, while high-energy ions provide significant atom sputtering. Therefore, low-energy ions may be important in reducing the defect density, and improving the overall crystalline quality of the nanoparticle produced. In Figure 13a the ion energy distribution function computed at the nanoparticle surface is reported for different gas pressures. For low pressures, IEDF has a beam-like shape, suggesting that the ion motion in the sheath around the particle is collisionless. At higher pressures, the ion collection by the particle is enhanced: ions that would miss the particle if the motion were collisionless

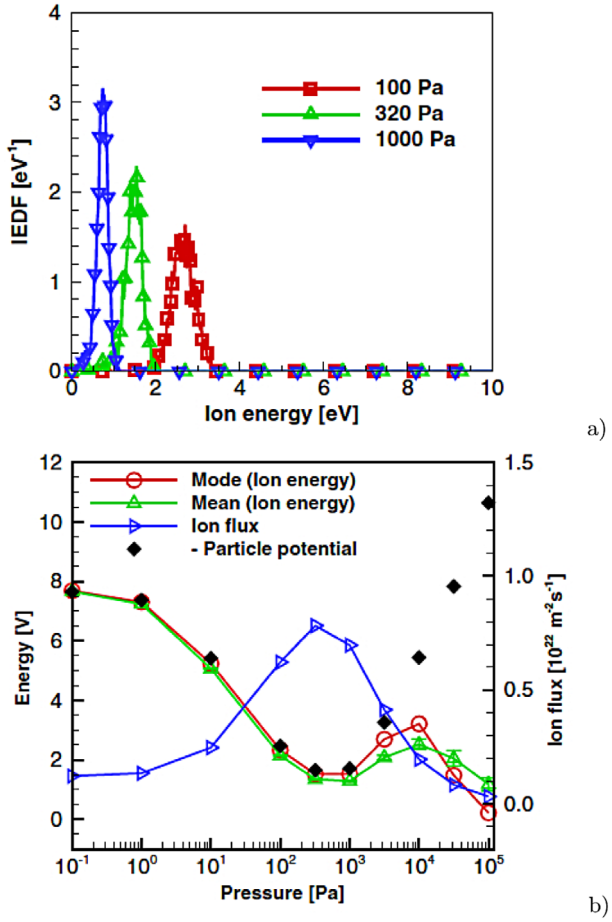

Fig. 13. (a) IEDF at the surface of 50 nm particles in a Maxwellian argon plasma with $T_e = 3.4$ eV and $n_e = 1 \times 10^{16}$ m^{-3} at three different pressures. (b) Nanoparticle potential (absolute value), ion flux and mean and mode for the energy of ions impacting on a 500 nm particle as a function of the gas pressure. The same plasma parameters are used [59].

do get collected by the particle since their angular momentum was changed in a CX collision. This leads first to an enhanced ion collection which causes a less negatively biased particle floating potential and thus reduced ion impact energies at the particle surface. Second, IEDF also develops a low-energy population, characteristic of ions that have undergone collisions within the sheath. As the pressure increases further, the ion motion in the particle sheath becomes strongly collisional, leading to a mobility dominated motion. In this hydrodynamic regime, the nanoparticle potential again becomes more negative, since collisions reduce the ion current to the particle. As a consequence the averaged ion impact energy starts to increase. Figure 13b shows the mean energy and ion flux as a function of gas pressure [59]. It is evident how in the intermediate pressure range both favourable conditions for the particle growth occurs: the mean ion energy reaches the minimum and the ion particle flux collected on the nanoparticle surface is maximum.

4.3 IEDF in CCRF discharge

As observed in Section 3.4 electron distribution function is important not only for determining reaction rates and sustaining plasma discharge in CCRF discharge, but to determine the voltage between plasma and surfaces, and then the bombarding ion energy. In this sense, IEDF plays a key role in the plasma-surface interaction for etching and deposition and for this purpose the ion flux-distribution function (IFDF) is more frequently used.

For low pressure and low-frequency (if the ion sheath transit time is much smaller than the RF period $\omega\tau_i \gg 1$) regime, the typical IEDF in CCRF discharge shows the bimodal shape [60]:

$$f(\varepsilon) = \frac{2N}{\omega\Delta\varepsilon}\left[1 - \left(\frac{2(\varepsilon - eV_{DC})}{\Delta\varepsilon}\right)^2\right]^{-1/2} \tag{19}$$

characterized by a distance between the two maxima

$$\Delta\varepsilon = \left(\frac{8eV_{AC}}{3\omega s}\right)\left(\frac{2eV_{DC}}{M}\right)^{1/2} \tag{20}$$

where the sheath voltage is assumed to have a sinusoidal behaviour $V_{sheath}(t) = V_{DC} + V_{AC}\sin(\omega t)$, s is the constant sheath thickness and N is the number of ions entering the sheath per unit time. The maxima of the IEDF correspond to the minimum and the maximum of the sheath voltage, respectively. In the high-frequency regime (transition from E-mode to H-mode [61]) or for increasing ion mass, the ions cross the sheath in a large number of radio-frequency cycles. The ions experience more or less the time averaged electric field rather than the instantaneous electric field. In this regime one obtains a narrow, beam-like IEDF. The presence of multiple double peaks is due to the presence of ions with different mass being $\Delta\varepsilon \propto 1/\sqrt{M}$. With increasing pressures, the bimodal shape successively disappears and the average ion energy decreases significantly due to low-energy peaks coming from secondary ions created by primary ion-neutral charge exchange CX collisions in the sheath.

Recent developments in the study of IEDF in CCRF discharges have focused on better controlling the IEDF and in particular the following knowledge has been acquired:

1. the full customization of the IEDF by using dual frequency CCRF to allow the control of ion flux and ion energy independently (electrical asymmetry effect EAE): the ion energy with the lower frequency and the ion flux with the higher frequency [62,63]; while the frequency determines the breadth of the IEDF, the tailoring of the driving voltage waveform adjusts the shape [64–66];
2. the effect of a spatially inhomogeneous magnetic field on the IEDF which has been shown to be similar to EAE; both effects act independently and they can work in the same direction or compensate each other [67].

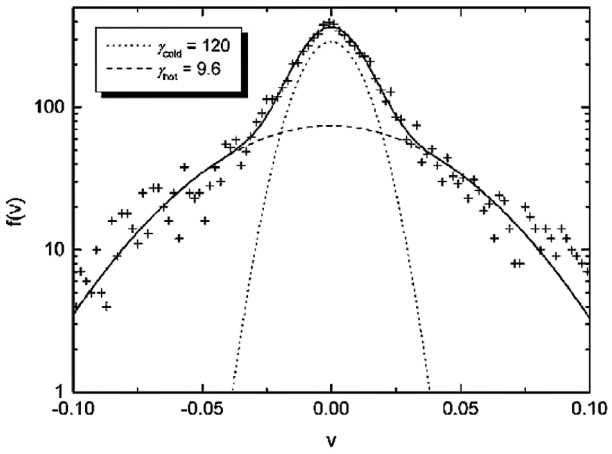

Fig. 14. A typical negative-ion velocity distribution function at the centre of the discharge for $\alpha = 3.1$ as result from hybrid PIC simulation [73]. ©2000 IOP Publishing Ltd.

4.4 Negative ion energy distribution function

Negatives ions are advantageous for several applications, e.g., Neutral Beam Injector (NBI) for controlled thermonuclear fusion [68], space propulsion [69], Dielectric Barrier Discharge for aerospace and medical applications [70], micro- and nano-electronic industry for etching, ashing, and oxidation, and other surface functionalization processes [71]. They are also at the basis of dust formation in plasma discharges.

It is generally accepted that negative ions are mainly produced by two different mechanisms [72].

In the volume by a two-step process that involves dissociative attachment of slow electrons $T_e < 2$ eV to highly vibrationally excited levels of molecules (see Sect. 5.3 for details). While often a Boltzmann relation with a fixed temperature is used to describe negative ions in electronegative discharges, the bulk negative-ion distribution function is found to have a bi-Maxwellian character with a cold and hot components $\gamma_{cold} = T_e/T_{-,cold}$ and $\gamma_{hot} = T_e/T_{-,hot}$. The typical steady-state negative-ion velocity distribution function at the centre of a low-pressure planar discharge is shown in Figure 14 for an electronegativity $\alpha = n_-/n_e = 3.1$. This result, coming from a hybrid kinetic model [73], where electrons are treated as fluid and positive and negative ions kinetically (see Sect. 7.3.2), can be qualitatively understood considering that negative ions born near the sheath edge will be accelerated by the electric field towards the centre of the discharge and thus gain substantial energy (of the order of kT_e). On the other hand, negative ions born in the central region where the electric field is small remain cold. Since negative ion collisionality is negligible, the time for negative ions to equilibrate greatly exceeds their life time.

The second mechanism involves the negative ion production by atomic/ionic conversion on low work function surfaces (often obtained by alkali or alkaline earth metal absorption to the surface). This mechanism is very efficient due to the proximity of the production to the extraction zone which reduces the negative ion loss probability. In negative ion hydrogen NBI system (NNBI), the surface-production increases the extracted negative ion current by a factor up to 6 [74]. The conversion yield $Y(\varepsilon)$ for ceasiated molybdenum surfaces (relevant to NNBI system in nuclear fusion reactor) strongly depends on energy of the impinging atom/ion, and presents an energy threshold of $\varepsilon_{th} = 0.72$ eV

$$\langle Y \rangle = \int_{\varepsilon_{th}}^{\infty} f(\varepsilon) Y(\varepsilon)\, d\varepsilon. \tag{21}$$

Therefore, for a high conversion rate, high atom flux and production of hot atoms are required. In this respect, it is essential the detailed knowledge of the translational distribution function of atoms $f(\varepsilon)$ produced in the bulk by the different molecular dissociation channels, by ion-atom charge exchange CX and/or on the wall by partial accommodation of the impinging ions. In reference [75], an high-energy tail has been detected by Monte Carlo simulation (see Sect. 7.3.1), which increases the total conversion yield from $\langle Y \rangle = 0.11$ (obtained with an equivalent temperature Maxwellian) to $\langle Y \rangle = 0.17$.

5 Molecular vibrational distribution functions

The vibrational degree of freedom in molecular plasmas or gas discharges performs a fundamental role in many aspects of plasma kinetics and applications. Much of the electron energy, up to 70–95% at low electron temperatures (around 1 eV), can be transferred to vibrational quanta, with a large effect on the energy balance of discharges. From the plasma chemistry point of view, endothermic reactions are greatly enhanced by the vibrational excitation of reaction partners (as already observed in Sect. 4.4 for negative ion production). A simple representation of the reaction rate coefficient of elementary reactions, in presence of vibrational energy E_v of at least one partner, is given by the formula (see Chap. 2 of [76] and references therein):

$$k_R(E_v, T_0) = k_{R0} \exp\left(-\frac{E_a - \alpha E_v}{T_0}\right) \Theta(E_a - \alpha E_v) \tag{22}$$

where E_a is the activation energy of the reaction, Θ is the Heaviside function. In this representation, the vibrational energy acts as to decrease the activation barrier. The quantitative details of such a decrease are included in the lumped coefficient α. The simple Fridman-Macheret model relates α to the activation energies of the direct and reverse reaction: $\alpha \approx E_a^D/(E_a^D - E_a^R)$. In general, then, α is high for strongly endothermic reactions and close to zero for exothermic ones. It is therefore immediately clear that a condition with $T_v \gg T_0$ greatly enhances endothermic reaction rates. As we shall see, in addition, strong non-equilibrium vibrational distribution functions (VDFs) deviating from a Boltzmann one, with large overpopulation of high v levels, can be found in gas discharges, with dramatic effects on reaction rates enhancement. We recall

at this point that molecular vibrations deviate from a harmonic oscillator, and that the oscillation energy can be expressed, as a function of the vibrational quantum number v as:

$$E_v(v) = \hbar\omega\left[\left(v+\frac{1}{2}\right) - \chi_e\left(v+\frac{1}{2}\right)^2 + y_e\left(v+\frac{1}{2}\right)^3 + \dots\right]. \quad (23)$$

The energy spacing between two adjacent levels is a decreasing function of v. To a first approximation, i.e. with the expansion stopped at the quadratic term:

$$\Delta E_v(v) = E_v(v) - E_v(v-1) = \hbar\omega(1-2\chi_e v). \quad (24)$$

The main sources of vibrational non-equilibrium will be addressed in the following.

5.1 Vibrational kinetics in plasmas

The book [77] is a classical reference for vibrational kinetics. More recent discussions can be found in references [2,36]. We address the reader to these books for a detailed and quantitative treatment. Here we only want to point out the physical grounds and the molecular basis underlying the build-up on non-equilibrium VDFs.

The v levels population can be calculated by solving a coupled set of differential equations for number densities N_v that we write formally:

$$\frac{dN_v}{dt} = \left(\frac{dN_v}{dt}\right)_S + \left(\frac{dN_v}{dt}\right)_{VV} - \left(\frac{dN_v}{dt}\right)_{VT} - \left(\frac{dN_v}{dt}\right)_R \quad (25)$$

in which source terms (S), redistribution without loss of vibrational quanta (vibration-vibration exchanges – VV) and loss terms (vibration to translation – VT – and chemical reactions R) are separated[1]. We shall now discuss briefly all the RHS terms, and see that all the terms are strongly dependent on v quantum number.

5.1.1 Vibrational excitation in plasmas

Electron impact is the main route of energy deposition into the vibrational manifold. It occurs preferentially into low v levels and by low energy electrons. Sample cross sections for nitrogen N_2 and carbon dioxide CO_2 are shown in Figures 15a and 16a. Corresponding rate coefficients as a function of electron temperature are reported in Figures 15b and 16b, showing that maximization of vibrational excitation can be achieved at electron temperatures of the order of 1 eV.

[1] An alternative approach is to treat the vibrational energy as a continuous variable, the VDF as a density in the energy space for which a continuity equation is written, where vibrational energy exchanges and losses are diffusion terms in the energy space (see Chap. 5 of [2] and references therein).

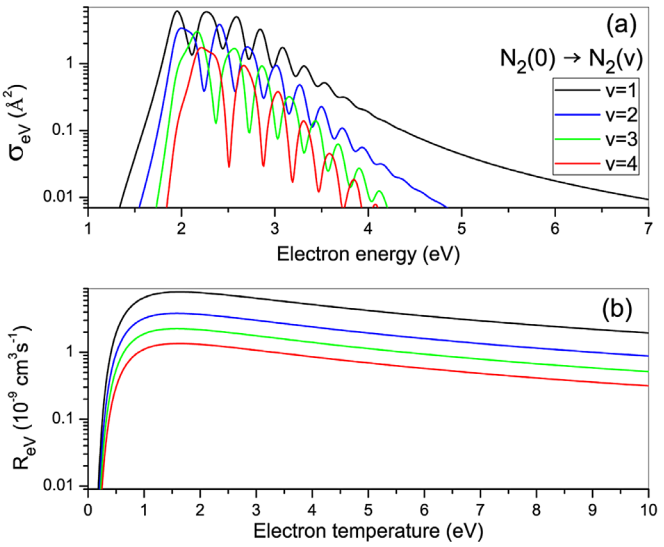

Fig. 15. (a) Cross sections for electron impact resonant vibrational excitation of low v states of nitrogen [78,79]; (b) corresponding rate coefficients, calculated for a Maxwellian EEDF, as a function of electron temperature.

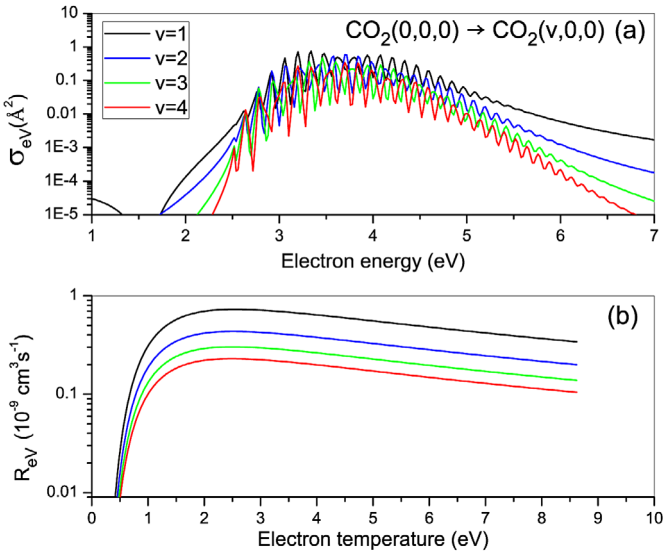

Fig. 16. (a) Cross sections for electron impact resonant vibrational excitation of low v states of the symmetric stretching mode of CO_2 [78,79]; (b) corresponding rate coefficients, calculated for a Maxwellian EEDF, as a function of electron temperature.

Further vibrational excitation can come from recombination and radiative cascade. Recombination processes, both in the gas phase and on a solid surface, accommodate much of the bond energy into vibrational modes, overpopulating high v levels. Provided parent atoms concentration is sufficiently high, i.e. a high dissociation degree is achieved in the discharge, this contribution can be important. An example of surface recombination nascent VDF is shown in Figure 17, for N recombination on a silica surface [80].

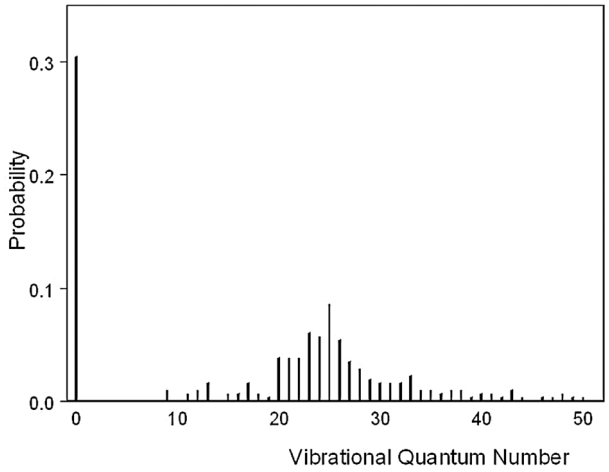

Fig. 17. Recombination probability and nascent N_2 VDF for the Ealey-Rideal N+N recombination on silica surface at 1000 K, with 0.055 eV kinetic energy of the impinging atom (from [80]. ©1991 Elsevier).

Radiative cascade after excitation of an electronic state (EV process) can be another important source of high v levels population. In the H_2 case (important for the design of H^- sources):

$$e + H_2(X, v) \rightarrow e + H_2^*(B, C) \rightarrow e + H_2(X, w) + h\nu \quad (26)$$

where the $B^1\Sigma_g^+$ and $C^1\Pi_u$ states are excited by electron impact, and radiative decay on $w > v$ levels occur with large probability (see [81] for a complete set of vibrational state-specific cross sections of H_2).

5.1.2 VT and VV relaxation

Vibration-to-translation (VT) relaxation includes all collision processes in which one or more vibrational quanta are lost in favour of kinetic energy:

$$\begin{aligned} M_2(v) + M_2 &\rightarrow M_2(w) + M_2 + \Delta\varepsilon_T \qquad \text{(VTm)} \\ M_2(v) + M &\rightarrow M_2(w) + M_2 + \Delta\varepsilon_T \qquad \text{(VTa)} \end{aligned} \quad (27)$$

where the collision partner is the molecule itself (VTm) or the parent atom (VTa). The treatment of multicomponent gases is straightforward. Rate coefficients can be calculated with various approximate methods, starting from the Landau-Teller formula (see [2]) to more complex ones for which we address the reader to Chapter 3 of [77] by Billing and to Chapters 3 and 8 of [36]. In general, VT processes are quite slow for low v levels, one-quantum losses ($v - w = 1$) are faster than multi-quantum ones, and show a strong dependence on the vibrational quantum number and on gas temperature. As an example we show in Figures 18 and 19 current data on VTm and VTa rate coefficients for N_2 molecule.

The VV transfer process is schematized as:

$$M_2(v) + M_2(w) \rightleftarrows M(v') + M(w') + \Delta\varepsilon_{nm}. \quad (28)$$

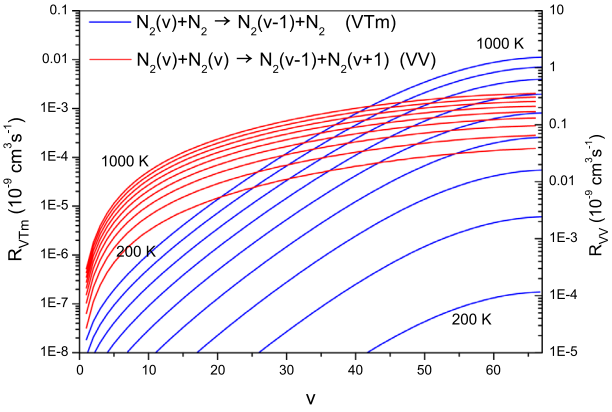

Fig. 18. Rate coefficients for one-quantum de-excitations in $N_2(v)$-N_2 collisions by VTm [82] (blue), and quasi-resonant VV (red) as function of v for gas temperature from 200 to 1000 K [83]. The data shown are obtained by fitting formulas [84] and are normalized to the whole vibrational ladder [85].

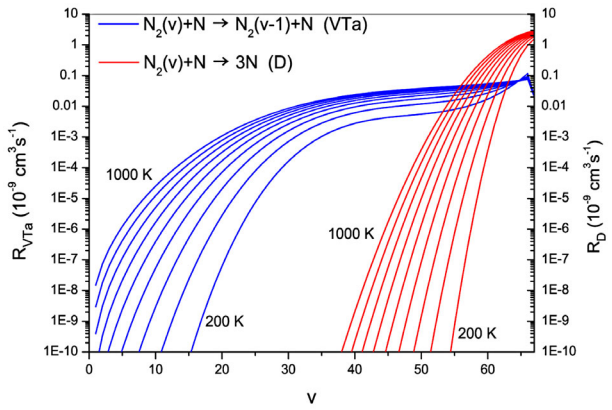

Fig. 19. Rate coefficients for one-quantum de-excitations in N_2-N collisions by VTa (blue) and dissociation (red) as function of v for gas temperature from 200 to 1000 K. QCT calculations [86] fitted by interpolation formula reported in [87].

VV transfers conserve the number of vibrational quanta, are faster than VT losses at low v values, and show a milder dependence on the vibrational level and on gas temperature. Again one-quantum processes are faster than multi-quantum ones, so we restrict our brief discussion to this simpler case. Numerical calculations of vibrational kinetics normally include also multi-quantum transfers. An example of VV rate coefficients as a function of v and gas temperature is shown in Figure 18.

VV transfers have a peculiarity capable of inducing a strong non-equilibrium in the VDF. Due to anharmonicity, VV processes have a non-zero energy defect, with the exception of the resonant transition – with $w' = v$ and $w = v' = v - 1$. For quasi-resonant VV processes we get a positive energy balance:

$$M_2(v) + M_2(v) \rightleftarrows M(v-1) + M(v+1) + 2\hbar\omega\chi_e \quad (29)$$

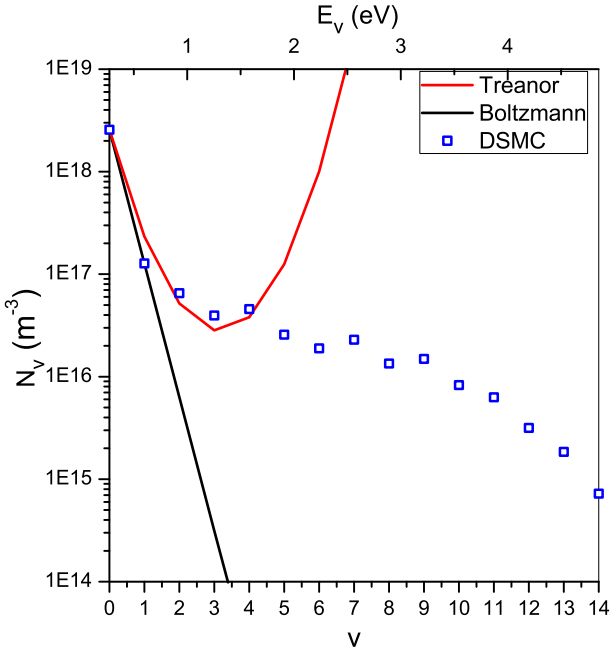

Fig. 20. Comparison between VDFs. Red line: Treanor distribution with $\Theta_1 = 0.18$ eV, $T_0 = 0.03$ eV, $\chi_e = 0.027$ eV (H_2 first order anharmonicity); black line: Boltzmann at $T_v = \Theta_1 = 0.18$ eV; symbols: DSMC calculations in an ICP H^- source operated at 0.6 Pa of H_2 and 170 W discharge power [68].

the rate coefficients for the direct, $k_{v,v}^{v-1,v+1}$, and reverse, $k_{v-1,v+1}^{v,v}$, reactions are then related by detailed balance:

$$k_{v,v}^{v-1,v+1} = k_{v-1,v+1}^{v,v} \exp\left[\frac{2\hbar\omega\chi_e}{T_0}\right]. \quad (30)$$

Given this relationship, the VDF that makes the VV flux equal to zero for each v, and in the absence of VT losses, is the Treanor distribution [88]:

$$N_v = B \exp\left(-\frac{\hbar\omega v}{\Theta_1} + \frac{\hbar\omega\chi_e v^2}{T_0}\right) \quad (31)$$

where B is the normalizing factor. The Treanor distribution has a minimum at $v_{min} = T_0/2\chi_e\Theta_1$ and, for small anharmonicity, $\chi_e \to 0$, or high gas temperature, $T_0 \to \infty$, it collapses into a Boltzmann one with a temperature $T_v = \Theta_1$. A comparison of Boltzmann and Treanor distributions is shown in Figure 20.

5.1.3 Chemical reactions

Vibrational excited molecules can promote chemical reactions that turn out to be loss processes for vibrational quanta at high v values. A common kind of reaction is dissociation:

$$M_2(v) + X + \Delta\varepsilon_v \rightleftarrows 2M + X. \quad (32)$$

An example is, for nitrogen, $N_2(v) + N \to 3N$, whose rate constant is reported in Figure 19, where it is shown that, at high v, dissociation provide loss rates comparable or larger than VTa ones.

Another kind of process, is the so called vibration to electronic (VE) reaction, in which vibrational energy promotes electronic excitation or ionization. Examples of such processes are:

$$CO(v = 40) + CO(v = 0) \to CO(A^1\Pi) + CO(v = 0) \quad (33)$$

$$CO(v) + CO(w) \to CO^+ + CO + e. \quad (34)$$

Process (33) was observed in reference [89], in which, after excitation of levels up to $v = 10$ by IR absorption of two CO laser photons, visible light emission from the $A^1\Pi$ state, the 4th Positive System, was observed. In reference [90] with the same IR absorption pumping, even CO ionization, process (34), was demonstrated. Both cases are a striking evidence of the efficiency of VV processes in populating high v levels.

Another example is, in nitrogen ([91] and references therein):

$$N_2(X, v \geq 5) + N_2(A^3\Sigma_u^+) \to N_2(B^3\Pi_g) + N_2(X) \quad (35)$$

that is responsible of the 1st Positive System (FPS) emission in the short lived (pink) afterglow (SLA) [92]. The SLA is an interesting case of interplay between VDF, metastable states and discharge kinetics. For a complete description of SLA kinetics see [93].

Note, finally, that all the listed processes, from the point of view of vibrational kinetics, are loss terms strongly dependent on v.

5.2 Vibrational distribution functions

Back to the kinetic equation (25), it is clear that analytical solutions are not possible, except with simple formulas for the rate constants and with approximations obtained in limit cases like those of weak or strong excitation (see Chap. 3 of [77] and, for the continuity equation approach, Chap. 5 of [2]). These approximations give useful qualitative information, but numerical calculations (see Sects. 7.2 and 7.3.1) are necessary for a quantitative approach, with the proper rate constants of all the relevant collision phenomena, and taking into account multi-quantum processes also.

The peculiarities of excitation, VV and VT processes allow to outline general qualitative features of non-equilibrium VDFs in plasmas. Excitation mainly occurs at low v levels and VV transfers tend to overpopulate higher v levels according to a Treanor distribution until VT losses start to be comparable and then larger than VV transfers. As a whole, and quite generally, VDFs can be thought as being composed of three parts on increasing v: the first part is roughly a Treanor distribution with a Θ_1 value that basically depends on the excitation rate; the second part is a quasi-plateau, where VV and VT conflict, and the third part in which VT dominate, with a fast decrease of the population of high v levels. One such example shown

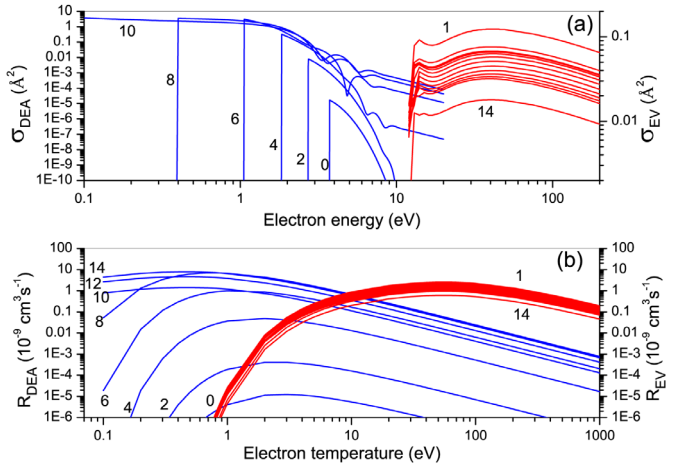

Fig. 21. Cross sections (a) and rate constants (b) for dissociative attachment (DEA), process (36) – blue curves, and radiative cascade (EV), process (26) – red curves. For DEA, curve labels are v level values. For EV the data refer to $v = 0$ and w ranging from 1 to 14. Data taken from [81,94].

in Figure 20, where the VDF of H_2 calculated by a Monte Carlo model (see Sect. 7.3.1) of an inductively coupled RF H^- source. The plateau extent depends on VT rates. In particular, since VT rates depend on the gas temperature and on the amount of atoms, in order to extend the plateau and achieve larger high v levels populations, conditions of low temperature and low dissociation degree must be pursued. In addition, the other state-selective processes mentioned in the previous paragraphs can give a further contribution to the final VDF shape.

The VDF dependence on the EEDF is evident through the rates of electron impact and radiative cascade excitation processes, and through the dissociation degree that affects VT rates. The reverse is also true, i.e. the vibrational excitation can in turn influence the EEDF by means of superelastic collisions. In Section 3.6 we have shown the influence on the EEDF of superelastic vibrational collisions in the CO_2 case (Fig. 7). We shall return on this specific case in the next paragraph.

5.3 Case studies

The influence of vibrational kinetics on practical applications of non-equilibrium discharges is well illustrated by the case of volume H^- negative ion sources for nuclear fusion technology. The starting point for maximization of H^- concentration is its main formation mechanism, the dissociative electron attachment (DEA):

$$H_2(X, v) + e \rightarrow H_2^- \rightarrow H(1s) + H^-(1s^2). \qquad (36)$$

The DEA cross section is strongly dependent on v: its value grows and its energy threshold decreases on increasing v, as shown in Figure 21a. Correspondingly, the rate constants increase with v and have a maximum for very low electron temperatures (Fig. 21b).

With H_2 VDFs like that shown in Figure 20, it is clear that non-equilibrium vibrational populations can enhance the DEA rate by orders of magnitude. Maximization of H^- production then requires a maximization of vibrational excitation and minimization of vibrational losses. Given that high v levels are mainly populated by EV [95], i.e. process (26), the relevant rates plotted in Figure 21b show that maximum EV rates occur at electron temperatures much larger than those for DEA maximum. This gave birth to the idea of the tandem source, with two space regions separated by a magnetic filter (see Sect. 3.3). The first region with high T_e for high vibrational excitation through EV, the second region at low T_e for DEA maximization. It is worth to mention the concept of temporal filter, in which the two conditions high/low T_e are not separated in space, but in time, as discharge and post-discharge regimes in a pulsed discharge [96]. It is also worth mentioning that H atoms deactivate high v levels by VTa, calling for a minimization of their concentration. By the way H atoms also destroy negative ions by the associative detachment $H^- + H \rightarrow H_2(v) + e$. A way to reduce H density is to use wall materials that enhance H recombination on the surface. Recombination, in turn, contributes to vibrational excitation. Details and the remainder of the long history of H^- sources can be found in references [72,97].

Another issue of great importance is CO_2 splitting in gas discharges. Carbon dioxide dissociation:

$$CO_2 \rightarrow CO + O \qquad (37)$$

that requires a dissociation energy of 5.5 eV, is followed by further reactions giving basically CO, O, O_2 and, at very high temperature, C products. Thermal shift of the reactions equilibrium requires high temperatures of about 2500–3000 K to get significant dissociation and product formation. Slow cooling would produce a return to initial concentrations through quasi-equilibrium steps back to room temperature. To preserve a significant fraction of products, CO in particular, a fast non-adiabatic cooling must be implemented. With thermal plasma systems, used in practice only as gas heaters, and even in case of ideal quenching (instantaneous cooling), the energy efficiency has a 43% upper limit [76].

Non-equilibrium discharges can achieve higher energy efficiencies, up to 90% [76], and simply do not present the cooling problem since CO_2 dissociation can be achieved at close to room temperature by electron impact and by vibrational excitation of molecules:

$$CO_2(X^1\Sigma^+, v \geq 21) \rightarrow CO(^1\Sigma) + O(^3P). \qquad (38)$$

The role of the vibrational dissociation mechanism was already recognized in low pressure discharges in the late 70's [76,77]. Nowadays, there is a large interest in atmospheric pressure discharges for CO_2 conversion into syngas, liquid fuels like methanol and added value chemicals in general [98]. The role of the vibrational mechanism, at atmospheric pressure as well, has been recently addressed and recognized by theoretical calculations in which a simplified vibrational kinetics of the asymmetric mode

is coupled to a Boltzmann solver [99,100]. In particular it is shown in these papers that in microwave discharges, the VDF achieves a strong non-equilibrium character similar to that of Figure 20, with electron temperatures close to those of the maximum of electron impact vibrational excitation shown in Figure 16. In such conditions, process (38) gives a major contribution, significantly increasing the energy efficiency of CO_2 dissociation. In dielectric barrier discharges (DBD) instead, the vibrational excitation remains low, most of the dissociation is due to electron impact, and the energy efficiency is much lower than in the microwave case. DBD discharges are in fact composed of many micro-discharges each of few tens of ns of duration, randomly distributed in space and time, such that the same volume of gas very unlikely undergoes more than a single micro-discharge event. As shown in [101], the short micro-discharge duration is unable to sustain VV build up of the VDF.

Two further processes, not considered in references [99,100], make the VDF act on the dissociation: (1) the increase of high energy electrons due to superelastic vibrational collision and (2) the participation of vibrationally excited molecules in the electron collision dissociation, both enhancing electron impact dissociation as a whole, as shown in reference [102].

All these theoretical results must be considered as semi-quantitative, due to the approximations in the treatment of the vibrational kinetics and in the VV and VT rates used (for a state-of-the-arts CO_2 vibrational kinetics see [103]). Nevertheless, their conclusions clearly show that the vibrational mechanism seems to be of fundamental importance for the enhancement of CO_2 dissociation energy efficiency in modern atmospheric pressure devices. We like to mention also that these devices very often implement heterogeneous catalysis stages that in turn may act as further sources of vibrational non-equilibrium by recombination processes.

6 Reactive intermediates: metastable states and radicals

Great abundances of reactive transient species are produced in NTP systems, that is why such devices have started the rich history of plasma chemistry. At relatively low input energies and room gas temperatures, radicals concentrations in gas discharges can be many orders of magnitude larger than the thermal equilibrium ones. Just as an example, OH concentration in an atmospheric pressure He-H_2O dielectric barrier discharge was found in reference [104] to be of the order of 10^{14} cm^{-3} with an electrical discharge power density of about 5 W cm^{-3} at a gas temperature of 380 K. For a quick glance at how much large this number is, consider that thermal equilibrium would require many thousand of degrees to approach it, while the atmospheric concentration of OH, in presence of photochemical source processes, is of the order of 10^5–10^7 cm^{-3}. A great number of radicals could be listed here, that play a role in many applications of gas conversion or material processing (see, for example [76,105]). The trend of the moment is a renewed interest in oxygen (ROS) and nitrogen (RNS) reactive species, including O, O_3, OH, N, NO…, mainly due to the emerging Plasma Medicine field [106], in addition to the more classical plasma assisted combustion [107,108] and atmospheric pollutants removal [109].

A special class of reactive, transient intermediate species is that of electronic metastable states. Electronically excited atoms and molecules carry individually a large amount of energy, with a great potential for chemical reactions. Nevertheless, they suffer rapid quenching by radiative decay, such that their abundance is not of great importance, although still supra-thermal. Metastable states, on the contrary, for which dipole radiative transitions are not allowed, can reach high concentrations and deliver their energy into chemical and ionization processes. The most encountered and studied metastable states are the helium triplet $He(2^3S)$, the nitrogen triplet $N_2(A^3\Sigma_u^+)$ and the oxygen singlet $O_2(a^1\Delta_g)$, this latter being commonly classified as one of the most important ROS species.

$N_2(A^3\Sigma_u^+)$, with about 6.2 eV of energy in its lowest vibrational state, can promote numerous chemical reactions on transferring its energy to molecular partners (see for a partial list [110]). For example, interacting with oxygen, it can excite, dissociate and produce nitrogen oxides:

$$\begin{aligned} N_2(A) + O_2 &\rightarrow N_2(X) + O_2^* \\ &\rightarrow N_2(X) + 2O(^3P) \\ &\rightarrow N_2O(X) + O(^3P) \\ &\rightarrow N_2O(X) + O(^1D) \\ &\rightarrow 2NO(X). \end{aligned} \tag{39}$$

These reactions can be very important. For example, in dry ozonizers, a significant amount of the ozone production is originated by oxygen dissociation from reactions (39) [111]. In a nanosecond pulsed discharge in atmospheric pressure air, up to 50% of O_2 dissociation was observed and attributed mainly to the same mechanisms with nitrogen metastable and B, C electronic states [112]. Another example is the role of nitrogen metastable in the decomposition of NF_3 in a dielecric barrier discharge in N_2/NF_3 gas mixture [113].

Large concentrations of reactive intermediates are rather a consequence of non-equilibrium. Metastable states can indeed provide a feedback to non-equilibrium itself. Superelastic collisions can influence the EEDF, as we have seen in Section 3.6, once metastables concentration gets sufficiently large. The charge balance rate can be strongly influenced by processes like: step-wise ionization, i.e. electron impact ionizations starting from a metastable state; Penning ionization,

$$G^* + M \rightarrow M^+ + e + G \tag{40}$$

in which $He(2^3S)$, with its 19.8 eV energy is particularly efficient for a large number of molecules; “pooling” ionization, like that involving a singlet nitrogen metastable, $N_2(a'^1\Sigma_u^-)$,

$$N_2(a') + N_2(a') \rightarrow N_2{}^+ + e + N_2(X) \tag{41}$$

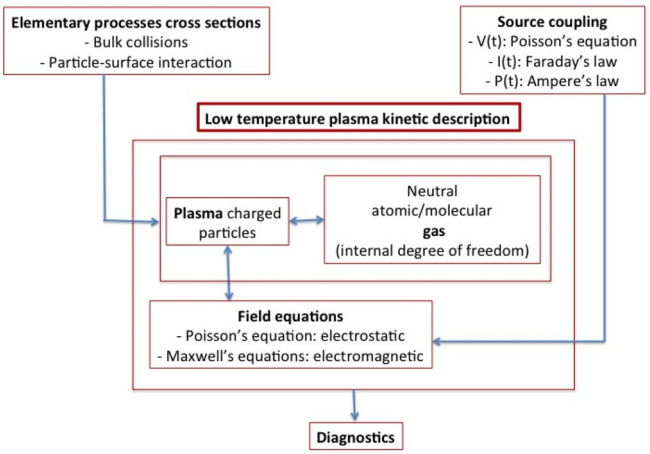

Fig. 22. Scheme of the different input data and couplings for a complete kinetic description of low temperature plasma system.

that is active in the already mentioned SLA (short-lived afterglow); secondary electron emission at the cathode of a discharge, due to metastable energy release to electrons of the metal surface, that contributes to the sustainment of the Townsend discharge mechanism. The latter mechanism, commonly accepted in low-pressure discharges, has been also invoked in a nitrogen atmospheric pressure DBD to explain the observed diffuse regime [114], where $N_2(A)$ densities as high as 10^{13} cm^{-3} have been found [115].

7 How to simulate plasmas in non-equilibrium: numerical models

A correct mathematical description of non-equilibrium condition can only be obtained from kinetic theory. The physical and chemical kinetics of charged plasma and excited gas particles requires many independent variables: coordinates, velocities of all the species and internal degrees of freedom (electronic/vibrational/rotational states) of heavy species. At the basis of all kinds of kinetic description is the knowledge of the cross section of the most relevant elementary processes involved. The different numerical approaches of BE solution, as result of interaction with electromagnetic fields, other particle species and boundaries, can be presented as a list of increasing complexity models. The different numerical approaches of BE solution, as result of interaction with electromagnetic fields, other particle species and boundaries (see Fig. 22), can be presented as a list of increasing complexity models. The recent book [116] represents a detailed work on the different numerical methods suitable for NTP simulation.

7.1 Swarms in neutral gas: polynomial expansion

For weakly ionized plasmas, the density of charge carriers is low in comparison with that of neutral particles. Thus, collisions of charge carriers with neutral particles have marginal influence on the velocity distribution function of neutral particles, which possess a Maxwellian velocity distribution. The problem is reduced to the solution of electron/ion distribution function with the knowledge of the collision cross sections and external forces.

A standard technique for solving BE (4) in this case consists in the separation of the space-dependence of the distribution function represented in terms of power series of density gradient operator (hydrodynamic regime):

$$f(\boldsymbol{x},\boldsymbol{v},t)=\sum_k f^k(\boldsymbol{v},t)\otimes^k(-\boldsymbol{\nabla})^k n(\boldsymbol{x},t) \qquad (42)$$

where $(\boldsymbol{\nabla})^k$ represents a k-fold outer product of the gradient operator with itself and $\otimes^k$ indicates a k-fold inner-product operation.

The second step is an expansion of velocity vector dependence of the distribution function ([117–120]) using spherical harmonics $Y_{ml}(\theta,\varphi)$

$$f^k(\boldsymbol{x},\boldsymbol{v},t)=\sum_{l=0}^{\infty}\sum_{m=-l}^{l} f^k_{ml}(\boldsymbol{x},v,t)Y_{ml}(\theta,\varphi) \qquad (43)$$

(θ and φ are the velocity angles) or Legendre polynomials $P_l(\cos\theta)$ if the direction of the force and the expected inhomogeneity are parallel to a fixed space direction z:

$$f^k(z,|v|,\cos\theta,t)=\sum_{l=0}^{\infty} f^k_l(z,|v|,t)P_l(\cos\theta) \qquad (44)$$

being $\cos\theta=\frac{v_z}{|v|}$. In contrast to the angular dependence of the distribution function in velocity space, many options are available for the treatment of the speed-dependence including finite-differencing schemes, polynomial expansions, pseudo-spectral methods, etc. In traditional kinetic theory, the expansion is made in terms of cubic B-splines [121] or Sonine polynomials [119]. The combination of spherical harmonics and Sonine polynomials represents the well known Burnett functions. Another basis set is tensorial Hermite polynomials used in the Grad thirteen-moment method.

Substituting expansion (43) or (44) into (4), BE is reduced to a set of coupled partial differential equations, one such equation for each expansion tensorial coefficient f_l of rank l. The set is solved as an initial-boundary value problem. Different finite difference method codes have been developed to solve the resulting set of equations for stationary discharge plasmas with zero, one, or two spatial dimensions as well as for time-dependent plasmas with zero or one spatial dimensions in hydrodynamic regime.

The collision term is separated in different contributions: elastic, inelastic (excitation, dissociation, etc.), non conservative (ionization, attachment, detachment, etc.) and binary Coulomb collisions.

The expansion is frequently truncated after the second term (known as two-term or Lorentz approximation), that is, $l=1$, and in case of Legendre polynomial expansion equation (44) becomes:

$$f(z,|v|,\cos\theta,t)=f_0(z,|v|,t)+f_1(z,|v|,t)\cos\theta. \qquad (45)$$

Here, f_0 is the isotropic part of the velocity distribution and f_1 is the anisotropic perturbation. This assumption is valid when cross sections for inelastic processes are much smaller than those for elastic processes. This condition is well met at low energies, for example, in the rare-gas atoms, for which electronic excitation requires several electron volts and for which the usual low-energy inelastic channels in rotation and vibration are absent. For diatomics or polyatomics, however, these two channels may be available for inelastic scattering at low energies so that the conditions required for the validity of the traditional two-term expansion may not be met. For high precision results, six or more expansion terms are needed. Among the different Boltzmann solvers based on the polynomial expansion approximation we can mention ELENDIF [122], PLASMAKIN [123] and BOLSIG [124].

7.2 State-to-state chemical kinetics models

When the coupling between plasma charged particles and neutral atoms and molecules becomes important, a more complete representation is needed. This is the case when the presence of vibrationally or electronically excited states of molecules and atoms strongly affects EEDF, since the super-elastic vibrational collisions tend to return energy to the electrons, thereby increasing the high energy portion of EEDF (as seen in Sect. 3.6). This is also the case when ion-atom resonance charge exchange collisions creates an important low energy ion population (see Sects. 4.1 and 4.2).

In these cases the solution of electron/ion Boltzmann equation is coupled with the atom/molecules internal degrees of freedom. A very common approach is the state-to-state non-equilibrium plasma kinetics [125]. It is a methodology which consists of considering the excited states of atoms and molecules as independent species with their own cross sections. It leads to a system of master equations, which describe the temporal evolution of the population densities of excited states under the action of collisional processes. In addition, when radiative processes (spontaneous emission and absorption and radiative recombination) are also important (for example at low ionization degrees), the so-called collision-radiative (CR) model is considered as an extension of state-to-state approach. In the case of an optically thin plasma in an atomic specie A, and considering only electron-atom coupling, the following direct and inverse processes should be taken into account:

1. excitation and relaxation by electron impact:

$$A(i) + e(\epsilon) \underset{k_{ji}}{\overset{k_{ij}}{\leftrightarrows}} A(j) + e(\epsilon'); \tag{46}$$

2. ionization by electron impact and 3-body recombination:

$$A(i) + e(\epsilon) \underset{k_{i,3b}}{\overset{k_{i,ion}}{\leftrightarrows}} A^+ + e(\epsilon') + e(\epsilon''); \tag{47}$$

3. spontaneous emission:

$$A(i) \xrightarrow{A_{ij}} A(j) + h\nu_{ij}, \quad i > j; \tag{48}$$

4. radiative recombination:

$$A^+ + e(\epsilon) \xrightarrow{\beta_{ij}} A(j) + h\nu, \tag{49}$$

where k_{ij}, k_{ji} and $k_{i,ion}$, $k_{i,3b}$ are the electron-impact rate coefficients (Eq. (2)) of excitation, relaxation and ionization, 3-body recombination processes, respectively, A_{ij} is the radiative transition probability and β_i is the radiative recombination coefficient.

The kinetic equations for the ith level population density (n_i) and for the electron (n_e) and ion (n_+) densities can be written as

$$\frac{dn_i}{dt} = \sum_{j>i} n_j A_{ji} + n_e \sum_{j\neq i} n_j k_{ji} + n_e^2 n_+ k_{ion} + n_e n_+ \beta_i - n_i \sum_{j<i} A_{ij} - n_i n_e \sum_{j\neq i} k_{ij} - n_i n_e k_{3b} \quad \forall i, \tag{50}$$

where electron n_e and ion n_+ densities come from the conservation equation

$$\frac{dn_e}{dt} = \frac{dn_+}{dt} = -\sum_i \frac{dn_i}{dt}. \tag{51}$$

The coupling with the electron system lies in the calculation of the different electron-impact rate coefficients equation (2), where the EEDF often comes from a 2-term expansion approximation of the BE.

In some cases, stationary solution or quasi-steady state (QSS) approximation can be used: in the first case all the temporal derivatives are set to zero, while in the second case, all the temporal derivatives of excited states equal zero, while the ground state is allowed to relax. QSS is valid for hydrogenoid systems characterized by much shorter relaxation times of the excited states compared to the ground state.

Diffusion and surface gain/loss terms can be added to the chemical process terms of the master equations (50) giving the reaction-diffusion equation:

$$\frac{dn_i}{dt} = D_i \frac{\partial^2 n_i}{\partial x^2} + \left(\frac{dn_i}{dt}\right)_{surf} + \left(\frac{dn_i}{dt}\right)_{chem} \tag{52}$$

where D_i is the diffusion coefficient of the atomic electronic level i. In optically thick plasmas, the inverse of processes (48) ane (49), i.e. absorption and photo-ionization, must be included. CR models assume that the mean photon free path is so short that all reabsorption happens at the same position of emission (local radiation approximation) and recent attempts have been proposed to couple CR model with radiation transport equation [126].

For molecular plasmas, the number of elementary processes to be included dramatically increases: electron-molecule excitation, dissociation and ionization cross sections, excitation and dissociation processes by atom and molecule interactions, VV and VT processes in molecule-molecule energy exchange processes and atom- and molecule-surface interaction processes must be considered.

7.3 Particle-based models

Particle-based models [127] represent the most sophisticated and powerful technique to reproduce the non linearity of a plasma kinetic system due to the different implicit couplings and interactions: plasma-gas, plasma-source, plasma-electromagnetic field, plasma/gas-surfaces. It consists first in decoupling the collective and collisional parts of the BE (4). Discretizing BE in time intervals Δt by neglecting terms of $\mathcal{O}(\Delta t^2)$ it leads to the following recursive rule:

$$f(\boldsymbol{x}, \boldsymbol{v}, t + \Delta t) = (1 + \Delta t C)(1 + \Delta t F) f(\boldsymbol{x}, \boldsymbol{v}, t) \quad (53)$$

which corresponds to splitting the evolution operator of the distribution function in two sequential parts: Monte Carlo (MC) [128] dealing with the collisional operator C and Particle-in-Cell (PIC) [129–132] dealing with the collective operator F, i.e. the motion between collisions. Both are based on the Klimontovich-Dupree discrete representation of the velocity distribution function in a cell (within which the plasma is considered to be homogenous) centred at $\boldsymbol{x}$:

$$f(\boldsymbol{x}, \boldsymbol{v}, t) = \sum_{i=1}^{N} \delta^3(\boldsymbol{v} - \boldsymbol{v}_i(t)). \quad (54)$$

7.3.1 Monte Carlo models

MC methods consist of tracking the motion of N particles under the effect of collisions with others particles (Direct Simulation Monte Carlo DSMC variant) or with a fixed distribution function background (Test Particle Monte Carlo TPMC variant). The influence of the Lorentz force, i.e. the electric and magnetic fields in the plasma must be regarded as given, and cannot be obtained in a self-consistent manner from the cooperative movement of the particles. The rules to process a collisional event are obtained substituting the representation (54) in the collisional operator; after some mathematical handling the probability for a collision to occur after the interval Δt is given by

$$P = n\sigma(v_r) v_r \Delta t \quad (55)$$

where n is the target density and v_r is the relative velocity with the collisional partner. P is compared with a random number R_{01} uniformly distributed between 0 and 1. If $P > R_{01}$ the collision occurs. Often, and in particular for electron-neutral collision, the target velocity is neglected and to speed up the calculation the null-collision method is adopted [133]. It consists to add a fictitious process to the set of real elementary collisions, maximizing the collision frequency in order to make it independent from the projectile velocity too:

$$\nu_{\max} = \max_{v}[n\sigma(v)v]. \quad (56)$$

This allows to select in advance a number of potential colliders $N_{coll}^{\max} = \nu_{\max} \Delta t N$ and check only for these particles if a real collision occurs. The random number R_{01} is compared with

$$P = \frac{n\sigma(v)v}{\nu_{\max}}. \quad (57)$$

In the same manner, the particular collisional event k contributing to the total cross section $\sigma = \sum_k \sigma_k$ is selected among the others with probability $P_k = \frac{\sigma_k(v)}{\sigma(v)}$. The knowledge of the angular differential and integral cross-sections allows the calculation of the azimuth φ and scattering χ angles, otherwise an isotropic scattering is set with:

$$\chi = \arccos(1 - 2R_{01}) \quad (58)$$

$$\varphi = 2\pi R_{01}. \quad (59)$$

The knowledge of collisional angles allows to know the post-collisional velocities based on the conservation of energy and momentum. Inelastic collisions are considered like elastic scattering with a loss term applied to the final energy. In case of ionization, the knowledge of secondary electron energy differential cross section allows to select the secondary electron energy.

Other types of collision processes, such as super-elastic collisions, recombination and attachment processes can also be incorporated in the MC scheme, as well as Coulomb collisions [134]. At very high ionization or attachment rates, re-scaling procedures may need to be applied [135] to keep a reasonable number of particles in the simulation.

Monte Carlo techniques are not only used for collisional events in the bulk but also for gas- and plasma-surface interactions once one knows the corresponding cross sections. Processes occurring at the boundaries (reflection, absorption, vibrational relaxation, associative recombination, ion neutralization, secondary electron emission [136], etc.) can also be accounted for in a straightforward way.

7.3.2 Particle-in-cell models

The addition of a spline function $S^{(n)}$ of order (n) for the space dependence in the Klimontovich-Dupree representation (54)

$$f(\boldsymbol{x}, \boldsymbol{v}, t) = w \sum_{i=1}^{N} \delta^3(\boldsymbol{v} - \boldsymbol{v}_i(t)) S^{(n)}\left(\frac{\boldsymbol{x} - \boldsymbol{x}_i(t)}{\Delta_i}\right) \quad (60)$$

corresponds to discretize the full phase space volume covered by the distribution function with single volumes (so-called macro-particles or virtual particles) every one characterized by its own position $\boldsymbol{x}_i(t)$, size Δ_i and velocity $\boldsymbol{v}_i(t)$, while w represents the weight, number of real particles contained inside the single volume. Substituting this representation in the collective operator part of BE (53), it leads to the equations of motion for the super-particles:

$$m_i \frac{d\boldsymbol{v_i}(t)}{dt} = q_i \left(\boldsymbol{E} + \boldsymbol{v_i}(t) \times \boldsymbol{B}\right) \quad (61)$$

$$\frac{d\boldsymbol{x_i}(t)}{dt} = \boldsymbol{v_i}(t). \quad (62)$$

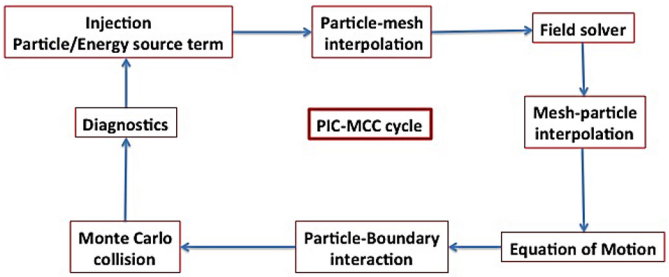

Fig. 23. The different modules of the typical PIC-MCC cycle.

The self-consistency with regards to the electromagnetic fields produced by the particles themselves consists in the calculation of electric $\boldsymbol{E}$ and magnetic $\boldsymbol{B}$ fields by solving the full set of Maxwell equations

$$\nabla \cdot \boldsymbol{E} = \frac{\rho}{\epsilon_0} \tag{63}$$

$$\nabla \cdot \boldsymbol{B} = 0 \tag{64}$$

$$\nabla \times \boldsymbol{E} = -\frac{\partial \boldsymbol{B}}{\partial t} \tag{65}$$

$$\frac{1}{\mu_0}\nabla \times \boldsymbol{B} = \boldsymbol{j} + \epsilon_0 \frac{\partial \boldsymbol{E}}{\partial t} \tag{66}$$

knowing the source terms, charge ρ and current $\boldsymbol{j}$ densities on a spatial grid:

$$\rho = q \int d\boldsymbol{v} f(\boldsymbol{x}, \boldsymbol{v}, t) \tag{67}$$

$$\boldsymbol{j} = q \int d\boldsymbol{v}\boldsymbol{v} f(\boldsymbol{x}, \boldsymbol{v}, t). \tag{68}$$

The latters are deposited on the mesh points by means of interpolation functions. The same functions are used to calculate the exact electric and magnetic fields at the macro particle position from the mesh points. Then, the equations of motion are solved and the velocity and position of every macro particles are updated. So the PIC cycle (represented in Fig. 23 with the MCC module) begins again.

Quite often PIC is used in the electrostatic approximation (the electric field comes from the Poisson Eq. (63)). Nowadays different fast numerical free software packages are available as Poisson's equation solver: HYPRE [137], FISHPACK [138], SuperLU [139], PETSc [140], WSMP [141]. In case of electromagnetic simulation the full Maxwell system is usually solved by finite-difference time-domain (FDTD) technique [142]. In case of RF-inductively coupled plasmas the full Maxwell's equations simplify considerably using the harmonic time dependence [143].

The Newtonian equations of motion (61)–(62) are most commonly solved by the finite-difference Leapfrog approximation scheme according to [127,129]

$$\boldsymbol{v}^{(n+1/2)} = \boldsymbol{v}^{(n-1/2)} + \frac{\boldsymbol{F}(\boldsymbol{x}^{(n)})}{m}\Delta t \tag{69}$$

$$\boldsymbol{x}^{(n+1)} = \boldsymbol{x}^{(n)} + \boldsymbol{v}^{(n+1/2)}\Delta t, \tag{70}$$

an explicit time-stepping scheme that is second-order accurate in both space and time. In case of magnetized particles, the Buneman-Boris variant is used.

The following constraints have to be imposed for an appropriate PIC-MCC model:

1. the cell size has to be of the order of the Debye length $\Delta x \sim \lambda_D$;
2. the time step has to resolve the plasma oscillations of electrons, i.e. $\Delta t\omega_{pe} < 0.2$ and in case of magnetic field, the electron cyclotron gyration $\Delta t\omega_{ce} < 0.35$;
3. the particles have not to cross a distance greater than the cell size during a time step (Courant condition): $\Delta t v_{\max} < \Delta x$;
4. in order to have a good statistics there should be a reasonably high number ($N_D \gg 1$) of particles present within a Debye sphere (ideal plasma);
5. the collision probability equation (55) should be kept reasonably small $P < 1$, to minimize the probability of more than one collisions of the same particle to take place during Δt.

Often, if the time and space scale interested are long enough to make electron reaching an equilibrium distribution, an hybrid approach can be used: ion and neutrals are considered as particles while electrons are treated as massless fluid equations. In place of solving the Poisson equation, a quasi-neutrality hypothesis is assumed and the electron conserving equation provides an equation of state (Ohm's law) for the electric field.

7.3.3 Molecular dynamics

By means of using a mesh for the self-consistent field solution, the number of operations per particle scales as $\mathcal{O}[\alpha N_p + \beta(N_g)]$ where N_p is the number of particles simulated and N_g the number of mesh points. For this reason PIC belongs to the particle-mesh PM methods. However, there are cases where the direct particle-particle force calculation is necessary to move the particle

$$m\frac{d^2\boldsymbol{r}_i}{dt^2} = -\nabla_{\boldsymbol{r}_i}\sum_{j\neq i}\frac{q^2}{|\boldsymbol{r}_i - \boldsymbol{r}_j|}. \tag{71}$$

It requires a much larger number of operations per particle $\mathcal{O}[\alpha N_p^2]$ that reduces the time and space scale investigated. These cases are typical of strong correlated plasmas characterized by a Coulomb coupling parameter (ratio between Coulomb energy and thermal energy)

$$\Gamma = \frac{q^2}{ak_BT} > 1 \tag{72}$$

(here $a = (3/4\pi n)^{1/3}$ is the Wigner-Seitz radius). Examples are high density and low temperature plasmas, as laser-induced plasma ablation in liquid or dusty plasmas (particles with an high value of charge). In these cases, the technique used is the Molecular Dynamics (MD), which is applied more frequently for liquid and solid phases. The statistical approach reduces to a deterministic approach

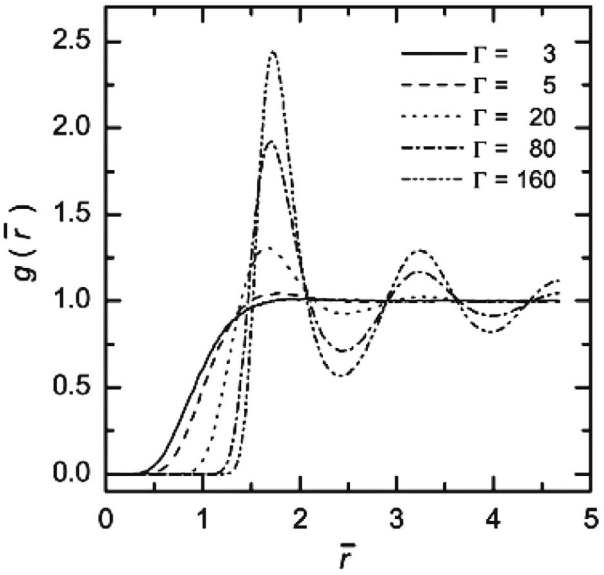

Fig. 24. Pair correlation functions of the classical 3D Coulomb OCP, for different values of the coupling parameter Γ. The distance is normalized by the Wigner-Seitz radius [144]. ©2009 IOP Publishing Ltd.

capable of bringing out the correlations between the particles going up in the BBGKY chain from the single-particle distribution function to a complete multi-body representation. Often, the one-component plasma (OCP) model [144] is used, where only one type of the plasma constituents is considered explicitly and regarded as collection of point charges while the oppositely charged particles are assumed to form a uniform background of neutralizing space charges. Figure 24 shows pair correlation functions (PCF) $g(r)$ for the 3D Coulomb OCP for a series of Γ values [144]. At high Γ, we observe very strong correlation in the particle separations corresponding to those of a bcc lattice. With decreasing Γ the peak amplitudes of $g(r)$ decrease, but the positions of the peaks remain nearly unchanged.

Even if the particle-based approach usually demands much more computation time than the solution of the kinetic equations, MC, PIC and MD models have greatly benefited from recent advances in high-performance computing. Parallelization techniques (MPI, OpenMP) and new computer architectures (GPU, MIC) associated with particle-decomposition and grid-decomposition allow to have nowadays fully kinetic three-dimensional real-scale device simulations with a speed-up factor of 60 compared to the serial PIC code for CPUs [145,146].

8 Experimental techniques

Almost all the degrees of freedom in a low-temperature plasma carry an element of non-equilibrium, as we have seen, and energy distribution functions show non-equilibrium features in frequent non-Boltzmann characteristics. The whole history of low-temperature plasma diagnostic techniques tells of a constant evolution towards the measurement of distributions, rather than temperatures. In this review, we shall pursue an abridged and up-to-date description of the main experimental approaches, addressing the readers to the many available reviews for the details of the techniques. In particular, we shall treat the measurement of: concentration and energy distribution of electrons, vibrational modes, transient species – radicals and metastable electronic states.

8.1 Electron density and energy distribution function

The electron component in a gas discharge is the carrier of energy taken from the electric field. Its energy distribution, EEDF, and density, determine the rates at which not only ionization, but all inelastic processes take place, including vibrational and electronic excitation and dissociation. Electrons are then the primary sources of non-equilibrium plasma chemistry, or, in other words, they have the leading role in the highly non-Arrhenius plasma catalysis. The measurement of the EEDF, or simply the electron temperature where applicable, is then fundamental for understanding mechanisms and for evaluating plasma chemistry initiation. It is also helpful in the design of plasma sources in which the EEDF can be somewhat tailored to the application requirements [1].

8.1.1 Langmuir probes

Langmuir probes have been serving the cause of plasma diagnostic for about 90 years, since when they were introduced by Langmuir in 1926. Within the endless literature on this subject, we direct the readers to two recent reviews that provide a complete description of the technique and an excellent basis for further reading [147,148]. In few words, a small metal piece – usually a thin wire – is placed into the plasma region and externally polarized by a voltage supply with respect to a counter-electrode. The latter, usually the grounded electrode in a discharge, is much bigger than the probe in the single-probe configuration. Application of the external voltage results in a potential difference between the probe and the plasma, V, and the electron current to the probe for a convex surface is given by the Langmuir expression:

$$I_e(V) = \frac{2\pi e S_p}{m^2} \int_{eV}^{\infty} (\varepsilon - eV) f_p(\varepsilon) dE \qquad (73)$$

where S_p is the probe surface. Calling *plasma potential*, V_s, the potential difference between the plasma and the counter-electrode, then $V = V_s - V_p$, where V_p is the external potential applied to the probe. Ideally, i.e. with infinitely large counter-electrode and zero resistance of the measurement apparatus, V_s is independent of the probe current. Double differentiation of equation (73) gives the well known Druyvesteyn formula:

$$\frac{d^2 I_e}{dV^2} = \frac{2\pi e^3 S_p}{m^2} f_p(\varepsilon = eV) \qquad (74)$$

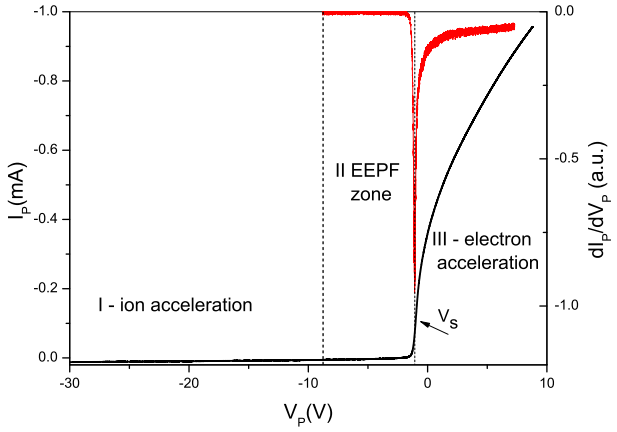

Fig. 25. Probe characteristic measured in the Inverse Brush Cathode (IBC) discharge of [149]. The current axis is inverted. The red curve is the first derivative of the current. The plasma potential is localized as the position of the minimum of the first derivative. The left limit of zone II is just pictorial.

providing a direct way for the measurement of the EEPF. In reality, the probe current is a sum of electron and ion current, $I_p = I_e + I_i$. A separation of the two currents is impossible in the electron retarding potential region. A typical $I_p(V_p)$ characteristic is shown in Figure 25. At the plasma potential, where the probe-to-plasma potential difference is zero, the transition occurs from electron retarding to electron accelerating regimes, that corresponds to an inflection point for the electron current, and, approximately, for the total probe current, since around this point the ion current is negligible. therefore at V_s the first derivative of the current has a minimum and the second derivative crosses zero. These features can be used to locate the plasma potential position, with some approximation as discussed in reference [148]. The zone II in the figure is where the EEPF is measured by formula (74). The main limit of the Druyvesteyn method at high electron energies is the difficulty in subtracting the ion current contribution, that adds up to the practical difficulty of measuring low values of the second derivative. The non-equilibrium in the electron component can be found not only in a temperature much larger than the ion and neutral ones, but also, and frequently, in non-maxwellian distributions. A collection of measured distributions can be found in reference [148]. Examples of state-of-the arts EEPF results by the second derivative method are reported in Figure 26, showing a high degree of non-equilibrium, with heavy influence on the electron impact inelastic processes that determine the ionization degree and plasma chemistry (dissociation). The bi-Maxwellian character, typical of CCRF discharge, as discussed in Section 3.4, can be observed for low gas pressure. As seen in the figure, a determination of the EEPF much above the ionization threshold, 24.58 eV for He, is difficult, due to the ion current limit of the Druyvesteyn method.

Finally, we mention that the electron/ion density can be derived by three methods: a) from the ion saturation current, provided the proper ion collection regime is identified [147]; b) from the electron saturation current, i.e. the current at plasma potential, that is equal to the random flux to the probe surface: $I_p(V_s) \approx I_e^{sat} = \frac{1}{4} S_p n_e \bar{v}_e$, with $\bar{v}_e$ = average velocity; c) by integrating the measured EEDF.

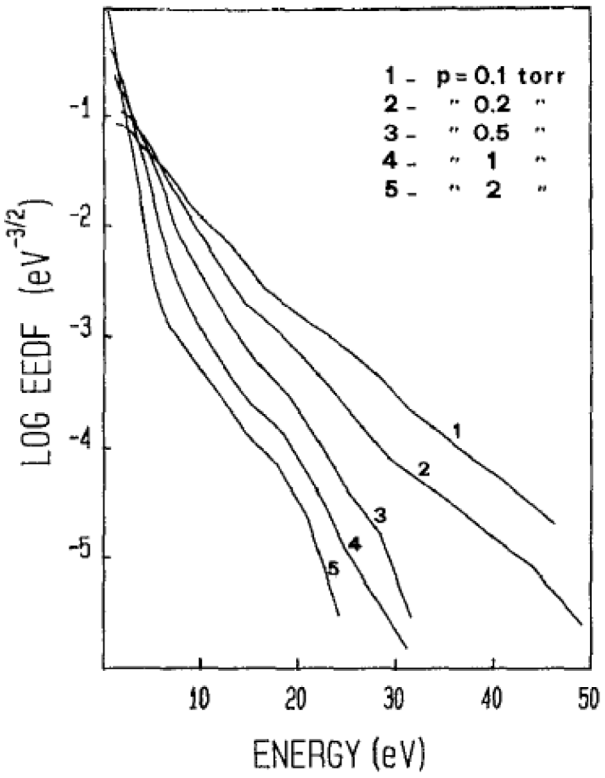

Fig. 26. EEPF measured in a capacitively coupled rf discharge in He at various pressures (from [150]) ©1991 American Institute of Physics).

8.1.2 Emission spectroscopy

Langmuir probes, although being in practice the only way for a direct EEDF measurement, and in addition to their many technical difficulties, are invasive and with a limited time response. Small size and fast transient events, although they carry strong non-equilibrium properties, are not in the range of probes applicability. Atmospheric pressure (ATP) discharges are the field where the need for capturing non-equilibrium features in the ns or sub-ns time scale, and in the sub-mm space domain, is of great importance. Emission spectroscopy has the technical capability to match these time-space resolution requirements. Modern intensified CCD detectors reach ns resolution, photomultipliers can have a 100 ps time response, and Cross-Correlation Spectroscopy has achieved tens of ps and 10 μm resolutions [151]. The information on the EEDF is, however, very limited. It is in fact based on the lines-ratio method, i.e. the measurement of the intensity of emission lines (or bands in the molecular case) originating from electronic states with different

excitation energy thresholds, in the case of electron impact excitation. In practice, a correct description of emission lines ratios requires a collision-radiative model (Sect. 7.2), that takes into account energy exchanges between excited states due to collisions with neutrals and electrons (see [152] and references therein). Complete and reliable data set are then needed, including excitation cross sections and collision rate constants. One such example is the CR model described in reference [153] for an Ar ATP discharge. For electron density above 10^{13} cm^{-3}, when electron collision processes start to overcome neutral collision ones, it was shown in a ns pulsed Ar microplasma that the line-ratio method can be used for the temporally resolved measurement of the electron density [154].

Back to the EEDF problem, the interval of the energy thresholds for electron impact excitations is the energy interval in which relative EEDF measurements can be achieved. In atomic gases, such an interval is very narrow, about 1–2 eV, and relevant to the high energy region just below the ionization potential. The classical nitrogen case offers a better possibility to the line-ratio method. The intense 2nd Positive System (SPS) of N_2: $C^3\Pi_u \rightarrow B^3\Pi_g$, and 1st Negative System (FNS) of N_2^+: $B^2\Sigma_u^+ \rightarrow X^2\Sigma_g^+$, are used to this end, with both $N_2(C^3\Pi_u)$ and $N_2^+(B^2\Sigma_u^+)$ excited by electron impact with ground state nitrogen molecules:

$$e + N_2(X^1\Sigma_g^+, v) \rightarrow e + N_2(C^3\Pi_u, v),\ E_{th} = 11.03 \text{ eV} \quad (75)$$

$$e + N_2(X^1\Sigma_g^+, v) \rightarrow e + N_2^+(B^2\Sigma_u^+, v),\ E_{th} = 18.7 \text{ eV}. \quad (76)$$

A discussion on the excitation/quenching parameters is given in reference [152]. The energy thresholds interval is quite large, but a model support for recovering the EEDF is essential. This is done by using a stationary Boltzmann solver, like BOLSIG+ [118] to calculate excitation rates at a given reduced electric field E/N. The condition of a quasi-stationary EEDF evolution is necessary, i.e. the electron energy dissipation frequencies [155] must be larger than the highest frequency of electric field change. Matching the experimental bands ratio gives the E/N value and the corresponding calculated EEDF. Note that, given the assumption of electron impact excitation, this method cannot be used in He-N_2 mixtures, where $N_2^+(B)$ is populated by Penning ionization from He(2^3S) metastable, or in Ar-N_2 mixtures, where $N_2(C)$ is populated by energy transfer from Ar metastable.

An example of time resolved nitrogen spectra is given in Figure 27, as measured in a single filament microdischarge in nitrogen at 50 Torr pressure. The band ratio corresponds to that of a stationary discharge with average E/N of about 540 Td. As it is seen, in electrical discharges the FNS emission is much less intense than the SPS one.

A feature of this spectroscopic scheme is that one of the two states is an ionic one, configuring a situation in which the two excitation cross sections have a fundamental difference, as it is shown in Figure 28: high energy electrons (> 100 eV) can produce intense FNS and no

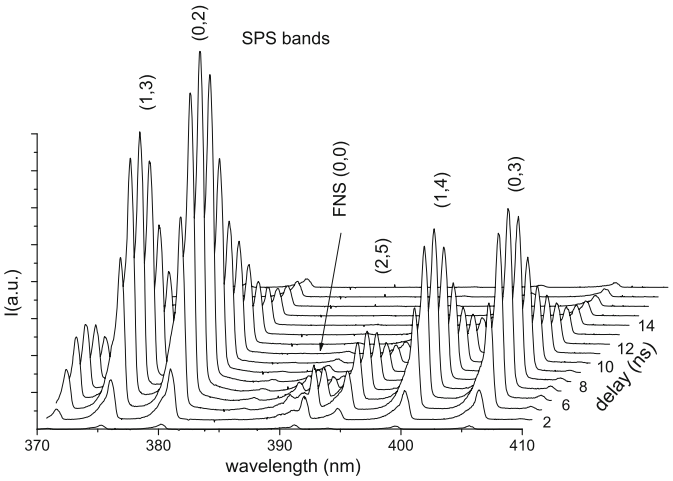

Fig. 27. Spectra measurements in a nitrogen microdischarge at 50 Torr, obtained by an intensified CCD synchronized to the voltage pulse (unpublished results. Courtesy of Šimek, IPP-AVCR, Prague).

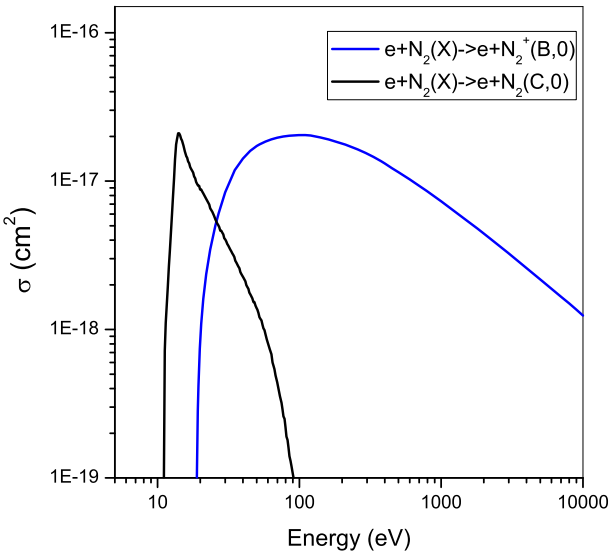

Fig. 28. Cross sections of processes 75 and 76.

SPS emission. In other words, the FNS/SPS intensity ratio can reveal extreme non-equilibrium conditions like that produced by a pulsed electron beam plasma. As shown in Figure 29, a monochromatic pulsed electron beam generates completely different emission spectra than those in a discharge. At the beginning of the pulse, no SPS emission is available, while, as time progresses, energy degradation of primary electrons and secondary electrons by ionization start to fill the low energy part of the EEDF, with a progressive increase of SPS emission.

Similar time resolved spectra were measured in a laser-target interaction experiment in low pressure nitrogen atmosphere [156]. In that case, the primary source of ionization was not an electron beam but the photo-ionization by extreme VUV emission of the laser-target plasma. The EEDF time evolution is equivalent to that of an electron beam plasma.

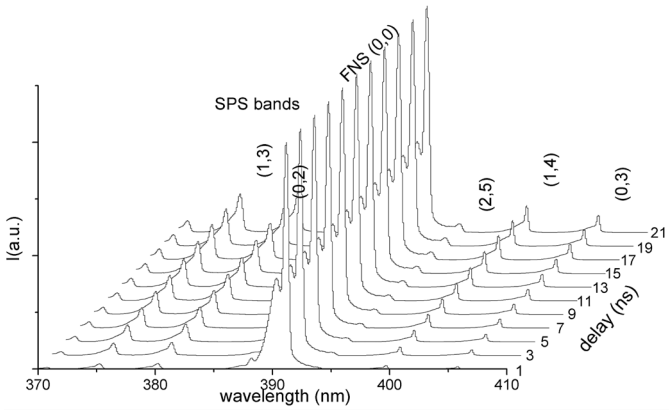

Fig. 29. Simulated spectra after Monte Carlo calculation of the EEDF produced by a 20 ns, 200 eV monochromatic pulsed electron beam propagating in nitrogen at 1 Torr (unpublished results. Courtesy of Longo).

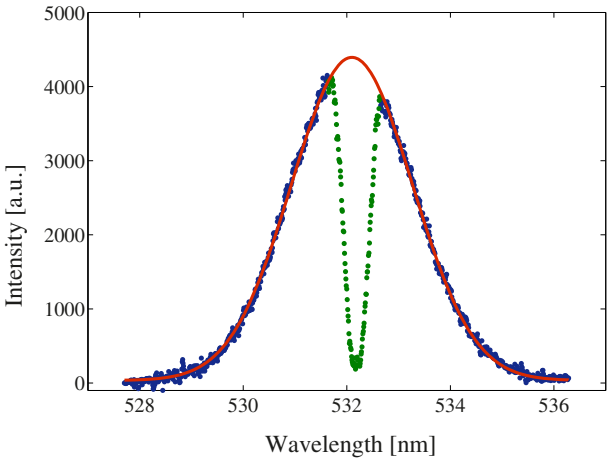

Fig. 30. Typical TS spectrum with spectral elimination of RS and stray laser light, in a microwave discharge in 20 mTorr of Ar. The detection makes use of a triple spectrograph, in which the first two monochromators act as a narrowband notch filter. The red curve is a Gaussian fit (purely Doppler broadening) from which T_e is measured. Accumulation over 18 000 laser shots (from [163]). ©2012 Institute of Physics Publishing).

8.1.3 Thomson scattering

A good collection of recent reference papers on Thomson scattering in electrical discharges is [157–160], and a review on the theory of light scattering can be found in reference [161]. The book [162] provides an up-to-date reference source on radiation scattering by plasmas. Laser light scattering by any particle is described by the general formula for the spectral power $P_\lambda(\lambda)$:

$$P_\lambda(\lambda) = P_0 \mathcal{C} n \left(\frac{d\sigma}{d\Omega}\right) \Delta\Omega S_\lambda(\lambda) L \qquad (77)$$

where P_0 is the incident power, n the particle density, $d\sigma/d\Omega$ is the differential scattering cross section, $\Delta\Omega$ the optical collection solid angle, L the collected length, $S_\lambda(\lambda)$ the spectral distribution normalized to unity, and $\mathcal{C}$ is a constant including all the experimental apparatus efficiencies. Elastic scattering is Thomson (TS) by electrons, Rayleigh (RS) by neutrals, and by molecules we have also inelastic Raman scattering. Cross sections are specific of the scatterer and of the process. The TS differential cross section is given by:

$$\frac{d\sigma^{TS}}{d\Omega} = r_e^2(1 - \sin^2\theta\cos^2\varphi) \qquad (78)$$

where r_e is the classical electron radius, θ the scattering angle and φ the angle between the laser polarization and the scattering plane. TS can be incoherent or coherent according to the scattering parameter α being much less or much larger than 1, where:

$$\alpha = \frac{1}{k\lambda_D}, \qquad k = |\boldsymbol{k}| = \frac{4\pi}{\lambda_0}\sin\left(\frac{\theta}{2}\right). \qquad (79)$$

$\boldsymbol{k} = \boldsymbol{k_s} - \boldsymbol{k_0}$ is the scattering vector, i.e. the vector difference between scattered and incident light, and $|\boldsymbol{k_s}| = |\boldsymbol{k_0}|$. In ordinary electrical discharges and with optical wavelength lasers, TS is incoherent, since λ_0 is much smaller than the Debye length. Therefore the scattered light is the sum of independent single electrons scattering events. The spectral distribution $S_\lambda(\lambda)$ is given by the Doppler broadening, both for TS and RS, such that the TS line broadening contains information on the EEDF. Experimental outcomes are the superposition of TS, RS and stray laser light. Most of the technical solutions for a good TS signal recovery and improvement of the lower detection limit are devoted to the reduction of stray light and to the separation of TS and RS signals. Since neutrals have a low kinetic temperature, the spectral width of the RS line is practically coincident with that of the laser light. RS and stray light can be removed by spectral filtering, as in Figure 30 [163] or subtracted as in Figure 31 [160]. The typical laser device used in TS scattering is a frequency doubled Q-switched pulsed Nd:YAG laser at 532 nm.

The lower detection limit, as discussed in reference [163], is characteristic of single cases of device geometry and plasma conditions. To cite rough numbers here, actual electron density limits are in the range 10^{11}–10^{12} cm^{-3}, while the electron temperature can be determined with high accuracy down to somewhat less than 0.1 eV. In reference [160] temperatures as low as 0.07 eV were measured. On the other hand, we are not aware of any non-Maxwellian EEDF detection by TS, due to the fact that the TS spectral wings are detectable just up to few eV of electron energy, i.e. at energies usually below the inelastic processes thresholds. In reference [164] it is shown that a combination of TS for low energy electron temperature, emission spectroscopy and a Boltzmann solver can be of help for EEDF determination including non-Maxwellian high energy tails.

Collective TS (CTS) requires a laser wavelength larger that the Debye length. This condition can be somewhat relaxed by designing a small observation angle θ (see Eq. (79)). As reminded in reference [159], CTS is not

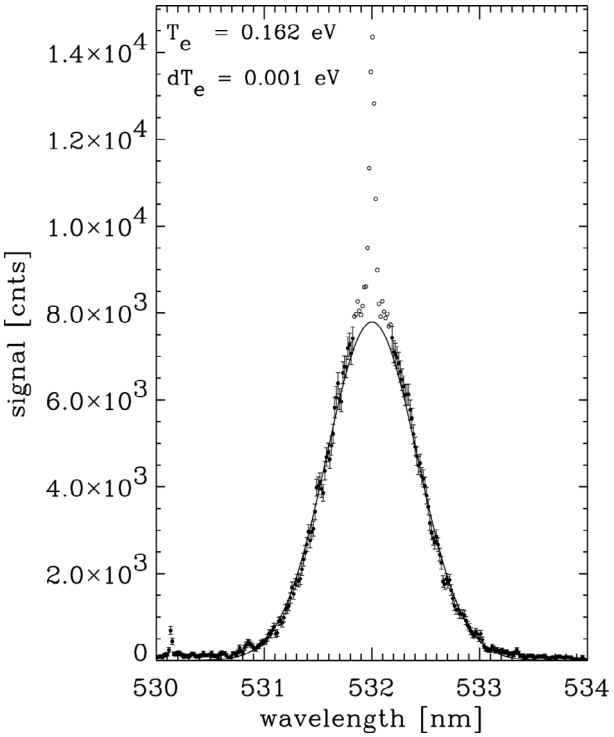

Fig. 31. TS spectrum with superposition of stray laser light, in an Ar expanding plasma at about 1 mTorr of Ar, $n_e = 1.2 \times 10^{13}$ cm^{-3}, with accumulation of 60 laser pulses only. The solid line is the fit from which n_e and T_e are determined. The data points centered around 532 nm (open circles without error bars) are excluded from the fit (from [160]). ©2012 American Institute of Physics).

as well studied as incoherent TS, and can be used, among other things, to determine the ratio between electron and ion temperature. In the same paper, the feasibility of CTS by a 1064 Å Nd:YAG laser with small θ is discussed.

8.1.4 Laser spectroscopy

We mention here another technique, the laser-collisional induced fluorescence (LCIF) for the measurement of electron densities higher than about 10^{11} cm^{-3}. A good summary of the technique and of its historical development can be found in [165]. LCIF is a laser induced fluorescence experiment in which, after populating an electronic state by absorption of laser photons, the observable is the fluorescence originating from states that have been populated by electron collision events. The principle of LCIF is illustrated in Figure 32, where it is sketched a possible (never used) scheme using He electronic states for which electron collision energy transfer rate constants have been measured in [166]. Fluorescence lines can be observed, among others, from 4^3P state (direct) and from 4^3D and 5^3D states (collision). 4^3P is populated by neutrals and electrons collision transfers, 5^3D by electron collision only, due to its higher energy that cannot be reached by thermal neutrals. Ratios of collision over direct fluorescence intensities give the electron density once the collision transfer

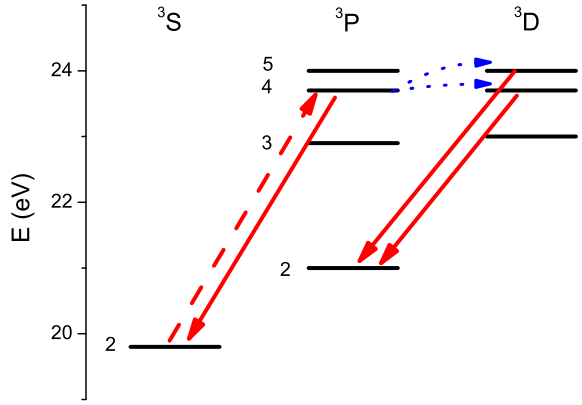

Fig. 32. He energy levels and possible LCIF scheme using the experimental setup and collision rate constants data of [166].

rate constants are known. Rate constants depend somewhat on the electron temperature. For a detailed discussion on available collision data and on the shape of the cross sections see [165]. A two laser-based diagnostics was proposed in [167] to measure n_e and T_e independently. Anyhow the LCIF method is sensitive to low energy electrons only, up to few eV, due to the cross sections energy dependence.

8.2 Vibrational distribution

Methods for the determination of vibrational levels population are all based on molecular spectroscopy. It is appropriate here to clarify that, from now on, we shall address vibrational distributions (VD) of ground, neutral molecules, that by far contribute the most to non-equilibrium bulk properties of molecular plasmas. One must avoid confusion with vibrational populations of electronically excited states, that often occurs when dealing with emission spectroscopy data. The basis of such methods is the anharmonicity of molecular vibrations. As we have seen (Eq. (23)), while in the harmonic case the energy difference between two vibrational levels is the same for all the transitions with the same $\Delta v = v'' - v'$, anharmonicity makes it possible to spectroscopically distinguish vibrational levels, since ΔE_{vib} depends on the couple (v'', v').

8.2.1 Infrared emission spectroscopy

Polar molecules emit infrared radiation as a consequence of vibrational transitions in the ground state. Appropriate choice of infrared transitions (fundamental $\Delta v = 1$, first overtone $\Delta v = 2\ldots$) against available IR detectors allows the measurement of IR emission spectra. Vibrational distributions can then be deduced, either by spectral simulation or by simplified formulas fitting the maxima of the spectra [168]. Distributions like that of Figure 33 are typical of a V-V up pumping, giving rise to Treanor-Gordiets shapes, competing at high v-levels with V-T quenching.

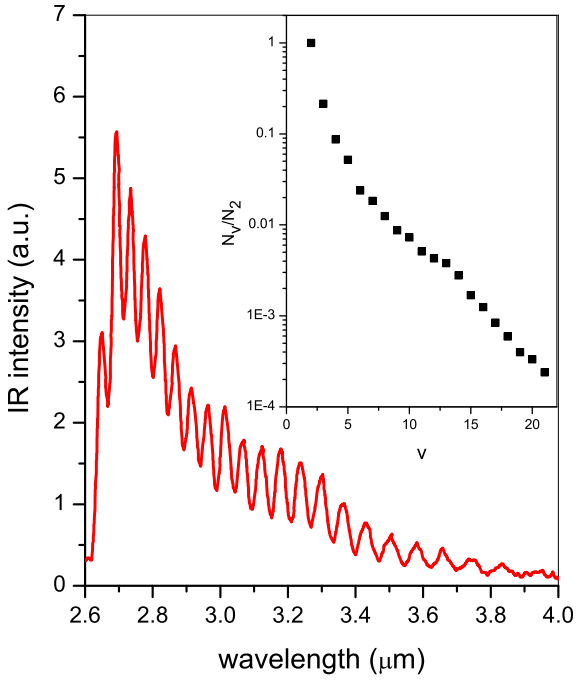

Fig. 33. First overtone IR spectrum of NO in a rf discharge [171] and (inset figure) NO(X, v) vibrational distribution calculated from the spectrum.

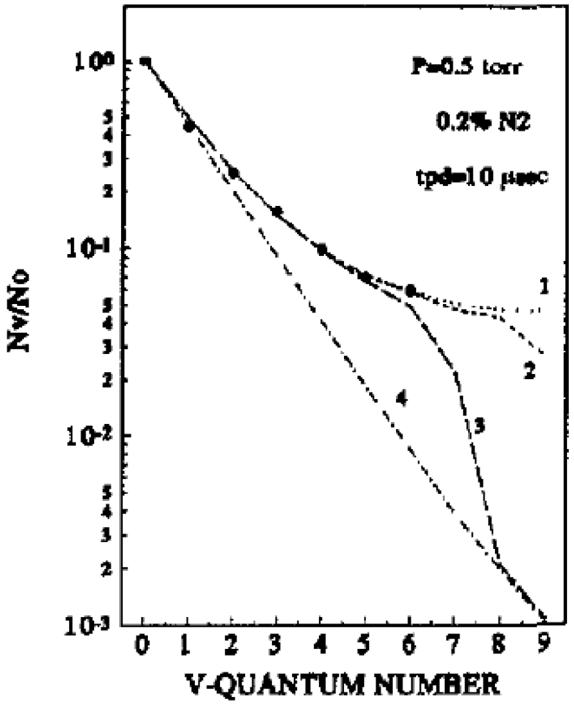

Fig. 34. $N_2^+(B, v')$ vibrational distribution measured at 10 μs in the post-discharge of a pulsed He-N_2 discharge. Simulations are obtained starting from $N_2(X, v)$ distributions: (1) Treanor-Gordiets, i.e. a Treanor distribution with $\Theta_1 = 4150$ K, $T_0 = 350$ K up to $v = 10$ and an exponential decay for $v > 10$; (2) and (3) modified Treanor-Gordiets (see original paper for details); (4) Boltzmann distribution at $T_v = 4150$ K (from [175]. ©1994 Institute of Physics Publishing).

Similar results were observed for CO distributions in a He-CO discharge [169], and the effect of gas cooling on V-T quenching was evidenced in reference [170]. Near-resonant vibrational transfer from N_2 to CO:

$$N_2(v) + CO(v-1) \underset{k_{v-1,v}}{\overset{k_{v,v-1}}{\leftrightarrows}} N_2(v-1) + CO(v) \qquad (80)$$

was shown as a mean of monitoring non IR-active N_2 vibrational distributions by looking at CO IR spectra [172], giving rise to further similar studies in references [168,170], in which CO was added downstream a nitrogen flowing afterglow. The vibrational transfer was then studied as a function of the contact time between discharge activated nitrogen and CO. This concept has been recently resumed in reference [173], in which CO, NO and N_2O molecules have been used as "IR titrating " molecules for the determination of wall deactivation probability of vibrationally excited nitrogen.

8.2.2 Optical emission spectroscopy

Indirect information on vibrational distributions can be inferred from optical emission spectroscopy provided the processes that populate the electronic emitting state are sufficiently well modelled. Here we just mention some results obtained from analysis of the nitrogen 2nd Positive System and 1st Positive System in a pulsed rf discharge [91,174] and in a Short-Lived afterglow [92]. In these papers, the vibrational excitation of electronic excited states, inferred from emission spectroscopy, were correlated to a number of discharge parameters, among which the $N_2(X, v)$ VD. Due to the complexity of the processes together with the uncertainty and underlying hypotheses of the state-to-state rate constants, these results are not to be considered as measurements, but rather as an estimate of the $N_2(X, v)$ distributions. In reference [91], for example, the $N_2(X, v)$ distribution was parametrized as a three temperatures one, approximating in this way a distribution shape similar to that of Figure 33. Results showed anyway a high degree of vibrational excitation and non-equilibrium. A more straightforward nitrogen VD recovery was obtained in a He-N_2 discharge in reference [175], using the 1st Negative System under the circumstance that, in presence of a huge amount of He triplet metastable, the emission was predominantly due to Penning ionization:

$$He(2^3S) + N_2(X^1\Sigma_g^+, v) \longrightarrow {N_2}^+(B^2\Sigma_u, v') + He + e. \qquad (81)$$

Being this a vertical Franck-Condon process, ground and ion B-state vibrational distributions are related to each other by the Franck-Condon factors matrix. The inversion of the matrix gives the ground state VD from the measured ion B-state VD. One such example is shown in Figure 34.

Infrared absorption spectroscopy can in principle be used also for the detection of vibrational quantum states, as in [173] by quantum cascade lased IR absorption. Its use for VDFs measurement is nevertheless unpractical

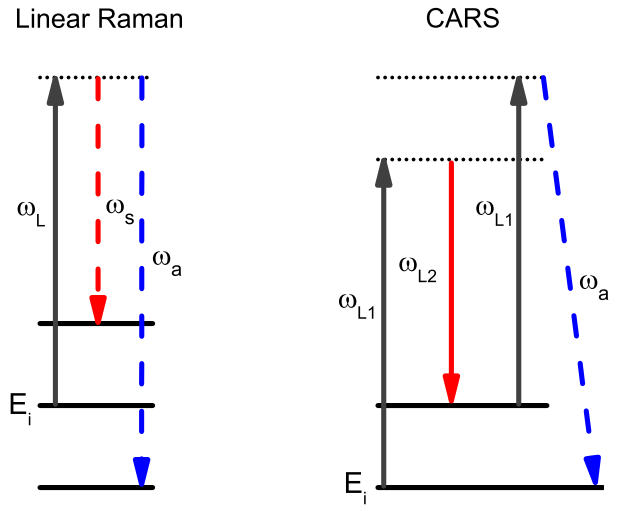

Fig. 35. Energy level scheme of linear Raman scattering and of CARS. Dotted lines represent virtual (non-stationary) states.

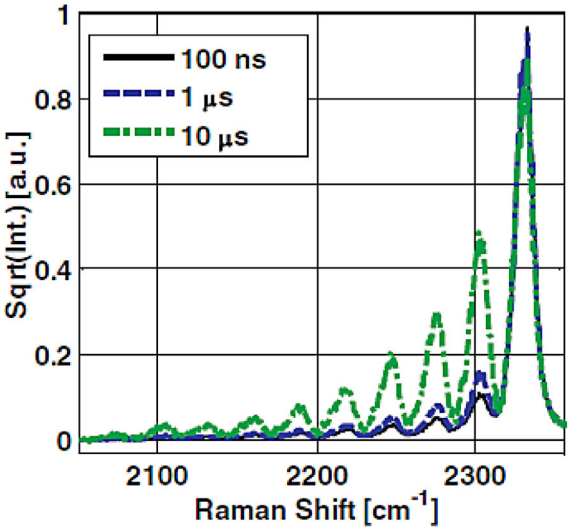

Fig. 36. CARS spectrum obtained in a 100 Torr N_2 pulsed discharge, with pulse duration of about 10 ns, and picosecond broadband laser (see text). Bands from levels $v = 0$–9 are clearly visible together with an increase of the vibrational population in the post-discharge due to radiative cascade from electronic states. The Raman shift abscissa is the value of $\omega_{L1} - \omega_{L2}$ (from [181]. ©2013 Institute of Physics Publishing).

due to the large spectral extension of the full vibrational manifold in the IR (see Fig. 33), and since the low transition probabilities require laser sources for cavity-enhanced absorption. At optical frequencies, instead, the larger probabilities of electronic transitions make it feasible, where available, the application of broad-band absorption (BBAS) with appropriate light sources. This has been reported in reference [176] for the O_2 VDF in a rf discharge, where absorption by the Shumann-Runge transitions has been observed across the 220–400 nm spectral range, using a recently developed broad-band source. Ground state vibrational levels up to $v = 18$ have been detected.

8.2.3 Laser Raman spectroscopy

Non-polar molecules, like N_2 and H_2 can be probed with spatial and high temporal resolution by laser Raman scattering. Linear (or spontaneous) Raman scattering is basically an inelastic collision of a photon with a molecule. For a general clue on Raman scattering as an interaction between an e.m. wave and a polarizable medium, see Chapter 8 of [177]. In terms of energy levels, referring to Figure 35, if the molecule is in a ro-vibrational initial state, the photon can loose or gain energy according to the final state being at higher or lower energy, giving rise to Stokes ($\omega_s < \omega_L$) or anti-Stokes ($\omega_a > \omega_L$) radiation. The intermediate state (dashed line in the figure) is normally a *virtual* one, resulting in very low scattering cross sections (order of 10^{-30} cm^2). In case it coincides with a stationary state, the Raman scattering is called *resonant*, and its cross section is orders of magnitudes larger. With a pulsed laser as light source, commonly a doubled Q-switched Nd:YAG at 532 nm, a whole ro-vibrational Raman spectrum can be measured by spectrally dispersed detection. Modern spectrographs equipped with sensitive intensified CCD (ICCD) detectors allow the recovery of the whole spectrum without the need of wavelength scanning. Unfortunately, in low pressure discharges the small Raman cross section does not allow the detection of non-equilibrium vibrational populations. At atmospheric pressure, instead, and with the aid of a long lasting laser pulse (about 100 ns, against the 10 ns of conventional Nd:YAG lasers), a successful application of the linear Raman technique has been demonstrated in reference [178]. In nanosecond repetitively pulsed (NRP) discharge in air for combustion applications, $N_2(X, v)$ populations up to level $v = 18$ were measured in reference [179], specifically in the post-discharge time. It was found a high vibrational non-equilibrium degree at the beginning of the post-discharge, relaxing to equilibrium with gas temperature in a 100 μs time scale.

At low pressure and at atmospheric pressure with a higher time resolution demand, Coherent Anti-Stokes Raman Spectroscopy (CARS) offers much larger sensitivity than spontaneous Raman, at the expense of a significant increase of equipment requirements. Two lasers are necessary to implement the scheme shown in Figure 35, one at fixed frequency ω_{L1}, the other, ω_{L2}, tuneable. The observable is the anti-Stokes radiation that appears as a coherent and collimated beam at $\omega_a = 2\omega_{L1} - \omega_{L2}$. The phase-matching condition $2\boldsymbol{k}_{L1} - \boldsymbol{k}_{L2} - \boldsymbol{k}_a = 0$ for the wave vectors of the three beams must be fulfilled, that is the condition for coherent growth of the anti-Stokes beam. The interested reader can find all the details and recent results of CARS in [180]. Here we just recall that scanning of ω_{L2} allows to measure a ro-vibrational spectrum covering a range of initial states.

In [181] use of a broadband dye laser allowed to avoid scanning of the laser wavelength. A low resolution vibrational CARS spectrum taken from this paper is shown in Figure 36. In the same paper, the time resolution

was pushed down to sub-ns scale by a 150 ps Nd:YAG laser used as the ω_{L1} source and to pump the dye laser.

In both low and high pressure cases a strong non-equilibrium has been observed by CARS measurements. In [182], in a nitrogen DC discharge at 4 Torr, an impressive dynamic range close to 10^3 allowed to detect vibrational populations up to $N_2(X, v = 14)$, showing distribution similar to that of Figure 33. A similar dynamic range was obtained in [181], but at 100 Torr, showing again strong non-equilibrium in a short time scale, evolving towards equilibrium in a hundreds of μs time scale, as in [179]. It is worth here to mention the CARS measurement of $H_2(v)$ in a magnetic multicusp discharge at 100 mTorr for negative ion production reported in [183]. Further examples can be found in [180] and references therein.

8.3 Metastables and radicals

We have grouped metastable states and transient species (radicals) in this paragraph since the techniques for their detection and measurement are the same, namely absorption and laser induced fluorescence (LIF). Although it is always good to measure absolute densities, relative measurements can be sometimes helpful, especially in pulsed discharges, in which the time evolution in both the discharge and afterglow phases provide insight into the kinetics of transient species.

8.3.1 Absorption

The absorption process is described by the equation (according to the notation of [184], with the exception of the symbol for the radiance I_λ):

$$dI_\lambda(x,\lambda) = -\kappa(x,\lambda)I_\lambda(x,\lambda)dx \tag{82}$$

for the $I_\lambda(x,\lambda)$ absorbed by a thin slab dx with a wavelength-dependent absorption coefficient $\kappa(x,\lambda)$ (units m^{-1}). The latter can be written, extracting the wavelength dependence, as $\kappa(x,\lambda) = \kappa^L(x)\mathcal{L}(\lambda - \lambda_a)$, with λ_a center wavelength of the absorbing atomic or molecular ro-vibronic transition, and $\mathcal{L}(\lambda - \lambda_a)$ normalized to unity. In terms of absorption cross section and concentration of the absorber specie:

$$\sigma(x,\lambda) = \frac{\kappa}{N(x)} = \frac{\kappa^L\mathcal{L}(\lambda - \lambda_a)}{N(x)} = \sigma^L\mathcal{L}(\lambda - \lambda_a). \tag{83}$$

Spatial integration gives the Lambert-Beer law:

$$I_\lambda(l,\lambda) = I_\lambda(0,\lambda)\exp\left[-\int_0^l N(x)\sigma^L\mathcal{L}(\lambda - \lambda_a)dx\right] \tag{84}$$

for absorption over a length l. The spatial dependence is, as a first approximation, contained in the density $N(x)$ only. The cross section is given by

$$\sigma^L = \frac{h\lambda_a}{c}B \tag{85}$$

with B the Einstein absorption coefficient.

An up-to-date review of recent advances in absorption spectroscopy applied to gas discharges can be found in [185]. The nature of the light source determines the kind of absorption experiment. Since the fraction of absorbed light is very low, in a classical absorption scheme the source stability over long integration times (of the order of several minutes or more) is of fundamental importance. Double beam schemes, with simultaneous detection of a free light beam and the absorbed one, allows to take into account long term drifts of the source radiance. This was particularly important with arc discharge light sources, used to produce the VUV radiation necessary for the electronic transitions of radicals like OH, CH, CH_3, NO, CF_2. Nowadays LEDs down to 245 nm are available that ensure a much better stability, as well as the novel laser-driven, broadband lamp used in [176]. In gas discharges, and in case of electric dipole ro-vibronic transitions, plasma induced emission, superimposed to the absorption pattern, can severely interfere with the measurement, and must be duly taken into account by a further measurement step. In [104,186], in the peculiar case of a pulsed dielectric barrier discharge, a time resolved absorption technique was implemented to avoid plasma emission and to monitor almost in real time the LED source radiance. Gas temperature and line broadening are important parameters for a quantitative analysis. The temperature determines both the population of single rotational levels and the Doppler broadening. Collision broadening is significant at atmospheric pressure, and must be accurately known. Modern ICCD detectors and broadband light sources allow fast recovery of absorption that can easily cover the spectral range of a full molecular band. Absorption spectra are calculated by summing all the ro-vibrational lines contributions (RHS of Eq. (84)) of the band(s) enclosed in the spectral window of the source/detector. Examples of broadband absorption measurements in discharges can be found in [187] (CF_2 and C_2), [188] (CH_3) and [104,189] (OH). Broadband absorption is less sensitive than the narrowband one, but has the advantage of a simultaneous measurement of the rotational (gas) temperature, that, in the narrowband case must be measured by other means or by a time consuming wavelength scan. A further noticeable advantage of the broad-band scheme is the possibility to discriminate multiple absorbers by their spectral features.

Simple absorption experiments are of practical interest in gas discharges only when the absorption probability is sufficiently high, i.e. in cases in which electronic transitions are involved. The sensitivity of absorption spectroscopy (AS) can be improved by increasing the absorption length l by multi-pass schemes. The maximization of this concept is Cavity Enhanced AS (CEAS), in which the absorbing medium is inserted within an optical cavity made of a couple of high reflectivity mirrors. In such a way, photons can travel back and forth in the cavity up to 10^3–10^4 times before being lost and measured, increasing accordingly the equivalent absorption length. Such an impressive enhancement allows both a sensitivity increase and the use of IR vibrational transitions for the absorption. For a recent review on CEAS methods, see [190].

We like to mention here that the recent development of Quantum Cascade lasers has greatly increased the application of CEAS to a large number of molecules (QCLAS [191]).

CEAS, like single pass AS, is an intensity-dependent method, since it measures the intensity ratio between incident and transmitted light, and is generally implemented with continuous, coherent (laser) or incoherent, broadband light sources [192,193]. A time-dependent version of cavity-enhanced AS is the Cavity-RingDown Spectroscopy (CRDS) [194], implemented with pulsed or modulated CW lasers (see [195] for a review). Pulsed monochromatic light is injected into a high-finesse cavity, and the light leaking from the cavity is measured by a photomultiplier. If the light bandwidth is sufficiently small as to match a single mode of the cavity, the measured ring-down light signal decays exponentially with a time constant given by:

$$\tau^{-1} = \frac{[(1-R)+\kappa l]c}{L} \tag{86}$$

where R is the mirrors reflectivity, L the cavity length, l the lenght of the absorbing medium placed inside the cavity. The observable of the experiment is then the decay time constant, so that the measurement is totally independent of the incident radiance, and is therefore robust even with respect to shot-to-shot radiance fluctuations. R determines the ring-down time constant τ_0 with empty cavity, i.e. with $\kappa = 0$. τ_0 marks the sensitivity limit of CRDS: the higher R, the longer τ_0 and the smaller the mesurable κ. A broad-band implementation of CRDS is also possible [196], which has basically to do with the analysis of a multi-exponential decay of the ring-down signal.

Cavity-enhanced absorption techniques have been used in gas discharges, for example, for the measurement of transient species such as: the nitrogen triplet metastable, $N_2(A^3\Sigma_u^+)$ in an inductively coupled low pressure discharge [197,198] and in a ns, atmospheric pressure discharge [199]; OH (UV CRDS on the A-X (0, 0) band at 308 nm [200], IR CRDS on the $X(v' = 2 - v'' = 0)$ band [201]); oxygen singlet $O_2(a^1\Delta_g)$ by near IR CRDS [202,203]; $He(2^3S)$ metastable in an atmospheric pressure plasma jet [204].

Absorption techniques provide absolute outcomes. Space and time resolution are not optimal. The space resolution is limited by the line-of-sight nature of absorption. The time resolution is generally low for non-laser schemes. Time resolution, where applicable, goes from the tens of μs of the BBAS scheme proposed in reference [186], with pulsed UV LED source and gated CCD detection, to the sub-μs one of reference [205], where resonant absorption was achieved by a pulsed discharge light source. Pulsed CRDS achieved a 50 ns time resolution in reference [199], but at the expense of sensitivity. Pulsed QCLAS has been reported with a time resolution down to about 1 μs [191]. Better space and time resolution, with comparable sensitivity, can be obtained by laser induced fluorescence.

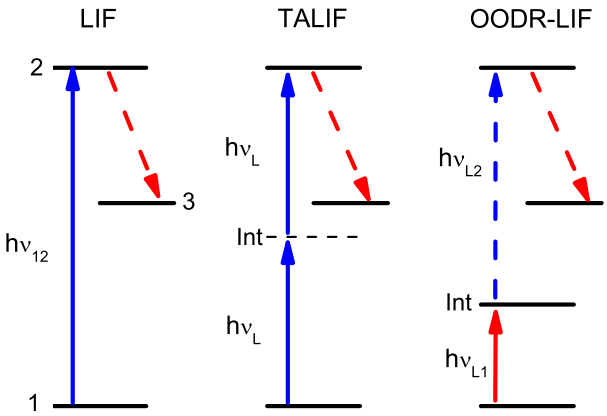

Fig. 37. Energy level scheme of single-photon LIF, TALIF and OODR-LIF.

8.3.2 Laser Induced Fluorescence (LIF)

Schemes of LIF processes involve ideally two atomic or molecular states coupled by an electric dipole transition excited by interacting with a quasi-resonant laser field (see Fig. 37). Level 1 is the probed state, while spontaneous emission from level 2 to a third level (the fluorescence) is the experimental observable. The transition to level 2 can be obtained in three ways: a) by absorption of a single photon, the simplest case; b) by absorption of two photons without a resonant intermediate state, or, in other words, with a virtual intermediate state, called TALIF (Two-photons Absorption LIF); c) by absorption of two resonant photons through a real intermediate electronic state, called OODR (Optical Optical Double Resonance) LIF. Use of any of the three schemes practically depends on the availability of proper electronic transitions.

The single photon LIF is generally applied to molecular species or to metal atoms or metastables. A generalized description of the technique and its application to diatomic radicals can be found in [206]. The LIF process is usually modelled by a set of rate equations (for a discussion on the validity of the rate equations model see [206] and references therein) that describe the time evolution of the populations of levels 1 and 2

$$\begin{aligned}\frac{dP_1(t)}{dt} &= -B\mathcal{E}_L(t)\psi(P_1(t)-P_2(t))\\ \frac{dP_2(t)}{dt} &= B\mathcal{E}_L(t)\psi(P_1(t)-P_2(t)) - (Q_2+A_2)P_2(t)\end{aligned} \tag{87}$$

while the population of level 3 is irrelevant to the process. The absorption rate is given by the spectral energy density of the laser field $\mathcal{E}_L(t)$, multiplied by the absorption coefficient B and the spectral overlap between the laser line and the absorption line Ψ. Level 2 population is lost by spontaneous emission with rate A_2, collision quenching with rate Q_2, and stimulated emission. Such a description is valid only if the two-level system is really isolated, and might be satisfactory in a collisionless environment, i.e. if collision rates that connect any of the two levels

to neighbouring ones are small compared with absorption/stimulated emission rates. At low pressure, roughly less than 1 Torr, this might be the case. When collision coupling of the two levels with neighbouring states is not negligible at high pressure, more complex model descriptions are required, as well as a detailed knowledge of the collision phenomena (see Ref. [206]).

Implementation of a LIF experiment in gas discharges calls for a time resolved LIF arrangement, both for practical reasons (namely the extraction of a short and large fluorescence pulse from a continuous plasma emission) and for capturing variations of species in fast discharge transients. Pulsed tuneable lasers with typical pulse durations of few ns (Dye, OPO, TiSa pumped by a Q-switched Nd:YAG or an excimer laser) are the standard equipment for LIF in gas discharges. This is then the time resolution of a LIF sampling, that can be further shortened by use of ps lasers.

The possible fluorescence outcomes are: (1) the time-resolved, spectrally integrated fluorescence pulse $S(t)$, measured by a photomultiplier (PMT) and a digitizing oscilloscope (DSO); (2) the spectrally resolved, time integrated fluorescence spectrum $I(\lambda)$, captured by an ICCD:

$$S(t) = CV_s A_{23} P_2(t)$$
$$I(\lambda) = \int_{t_1}^{t_2} S(\lambda, t)dt \tag{88}$$

where C is a constant including all the fluorescence collection, transmission and detection transfer functions, and V_s is the sampled volume. V_s, that determines the space resolution of LIF, is the intersection of the laser beam with the optical projection of the pinhole/slit entrance of the detector. Both can have a lateral size of the order of 100 μm.

The two photons for a TALIF scheme can be of different wavelength, but only cases with two equal photons of the same laser beam have been applied in gas discharges to the measurement of non-metallic atoms ground state species. For metallic ones single-photon schemes are readily available. With a single laser then $\nu_{12} = 2\nu_L$. Details on TALIF technique can be found in [207–209]. The rate equations model for TALIF is the same as that for single photon, in which the absorption rate is calculated as follows:

$$R(t) = \sigma^{(2)}\psi(\Delta\nu)G^{(2)}\left(\frac{I_L(t)}{h\nu_L}\right)^2 \tag{89}$$

in which, as it is customary in the literature, the energy density and the absorption coefficient are equivalently replaced by the laser irradiance $I_L(t) = c\mathcal{E}_L(t)$ and by the absorption cross section, respectively. $\sigma^{(2)}$ is the two-photon absorption cross section (in cm^4), $\psi(\Delta\nu = 2\nu_L - \nu_{12})$ is the overlap integral (see [207]). The pumping rate is proportional to the square of the laser field (intensity). $G^{(2)} = \langle f^2(t)\rangle/\langle(f(t)\rangle^2 = \langle f^2(t)\rangle/F(t)^2$, where $f(t)$ is the *true* laser pulse profile (i.e. the profile that would be measured by a sufficiently fast detector as to capture all its time variations) and $F(t)$ the measured averaged profile. This factor is necessary since fluctuations of the laser intensity cannot be simply averaged due to the non-linear dependence on the irradiance. Even measuring shot-by-shot the time profile of the laser beam, fluctuations occurring in a time scale shorter than the response time of the measurement (and longer than the coherence time) are anyway averaged in the measurement of $F(t)$. For multimode lasers like those used in pulsed LIF experiments, $G^{(2)}$ tends to 2, the value for cahotic light [210]. C, Cl, F, H N, O, S I, Xe atoms have been detected by TALIF with laser wavelength in the range 205–305 nm (except for fluorine at 170 nm). Two-photon absorption cross sections are very small, of the order of 10^{-35} cm^4, calling for high laser irradiances. The laser beam is then focussed. The high irradiance of focussed beams opens the way to two more processes: three-photons ionization, due to absorption of a third photon by level 2, and Amplified Spontaneous Emission (ASE), that occurs when a sufficient population inversion is created between states 2 and 1. They introduce a strong non-linearity in the LIF signal as a function of I_L^2, such that increasing I_L starts to be disadvantageous after a certain value [211,212].

When the intermediate state is a resonant electronic state, the two-photon absorption rate considerably increases. OODR-LIF belongs to the *pump-and-probe* class of experiments aimed at the investigation of the ro-vibrational relaxation dymanics of the intermediate state [177]. Its use for analytical purposes may be useful at high pressure for the selection of a level 2 state with better quantum yield. To the best of our knowledge, the only case reported in literature is that of OODR-LIF detection of $N_2(A^3\Sigma_u^+)$ metastable state [115], with $N_2(B^3\Pi_g)$ as intermediate state and $N_2(C^3\Pi_u)$ as final state (level 2). Such a scheme features a quantum yield, and then a signal outcome, about 10^2 times larger than that of the single photon scheme in which the final state is $N_2(B^3\Pi_g)$. Results reported in reference [115] show far from equilibrium $N_2(A^3\Sigma_u^+)$ concentrations as high as 10^{13} cm^{-3} in a nitrogen dielectric barrier discharge at atmospheric pressure. It was pointed out also the role of metastable states in sustaining a Townsend diffuse discharge mode in contrast to a randomly filamentary one, an intriguing case in which microscopic non-equilibrium kinetics is able to influence the macroscopic behaviour of the discharge.

Finally, we note that in all three LIF cases, and especially in the last one, a calibration method is highly desirable, if not strictly necessary. It is most often a different concentration measurement method applied in a reference condition. A summary of LIF calibration strategies can be found in reference [213].

9 Conclusions

The non-equilibrium of non-thermal plasmas, whose basic features we hope to have clarified in this paper, is what makes them attractive for technological applications. Sometimes NTP technologies are unique, sometimes they must compare with other existing/possible

competitors. The battlefield of such a competition is energy efficiency and process selectivity. On the other hand, the physical system turns out to be very complex and hard to govern. Non-linearity, inhomogeneities, transient phenomena, self-organized structures, are ubiquitous in NTPs. The molecular basis of non-equilibrium calls for a state-to-state knowledge of microscopic processes. Such a knowledge is necessary to face, and hopefully win, the technological challenges. Keeping in mind that each application is a singularity requiring specific research and optimization strategies. Given for granted that applications are the ultimate motivation for further efforts, one might wonder if this field is still worth of research investments. A quite complete map of actual and immediate future fields of NTP applications has been given in reference [214]. Although more classical cases like microelectronics, negative ion sources, electric thrusters, are still under intense investigation, recent progresses in atmospheric pressure discharges are now giving renewed impulse to basic and applied research, pushing both modelling and diagnostic techniques towards new limits in terms of spatio-temporal resolution. Pollution abatement, CO_2 disposal/valorization into value-added chemicals, plasma assisted combustion, plasma medicine, are all fields with high potentiality of societal impact, and all calling for improvements and enlargements of the actual investigation capabilities.

The need for basic data, physical insights and device control is then urgent and of fundamental importance even from the purely applicative point of view. For those who have been living the adventure of NTP research for a long time, such an urgent request appears to be today the same as it was 30 years ago. But looking backwards at that time, we cannot but recognize the enormous progress made, thanks to important developments both in numerical modelling and experiments, due to the progress done in high-performance computing and in diagnostic and discharge technologies. Progressive fine improvements have been realized: the space and time scales investigated have been increased; simulation domains have evolved from reduced dimensionality small zoomed region to the three-dimensional full scale device; the number of processes, with the corresponding knowledge of cross sections and rate coefficients, increases with the detail of state selection; diagnostic methods have been improved, while introducing new, very powerful, laser based techniques; discharge systems have evolved towards reliable, solid-state high power pulsed devices. The unchanged need of basic knowledge is then not the symptom of a stagnation, but on the contrary, the consequence of an increased consciousness of the system complexity, and of the vital impulse towards the expansion of all the capabilities of NTP technologies.

References

1. V.A. Godyak, Phys. Plasmas **20**, 101611 (2013)
2. A. Fridman, L. Kennedy, *Plasma Physics and Engineering* (CRC Press, 2011)
3. V. Pierrard, M. Lazar, Solar Phys. **267**, 153 (2010)
4. I.D. Kaganovich, Y. Raitses, D. Sydorenko, A. Smolyakov, Phys. Plasmas **14**, 057104 (2007)
5. D. Sydorenko, A. Smolyakov, I. Kaganovich, Y. Raitses, IEEE Trans. Plasma Sci. **34**, 815 (2006)
6. F. Taccogna, G. Mizzi, Contrib. Plasm. Phys. **54**, 877 (2014)
7. F. Taccogna, Eur. Phys. J. D **68**, 199 (2014)
8. A.I. Morozov, V.V. Savel'ev, Plasma Phys. Rep. **27**, 570 (2001)
9. J.P. Sheehan, N. Hershkowitz, Plasma Sources Sci. Technol. **20**, 063001 (2011)
10. G.D. Hobbs, J.A. Wesson, Plasma Phys. **9**, 85 (1967)
11. F. Taccogna, M. Longo, S., Capitelli, Phys. Plasmas **12**, 093506 (2005)
12. M.D. Campanell, Phys. Plasmas **22**, 040702 (2015)
13. M.C. Griskey, R.L. Stenzel, Phys. Rev. Lett. **82**, 556 (1999)
14. F. Taccogna, S. Longo, M. Capitelli, R. Schneider, Appl. Phys. Lett. **94**, 251502 (2009)
15. M.D. Campanell, A.V. Khrabrov, I.D. Kaganovich, Phys. Plasmas **19**, 123513 (2012)
16. A.I. Smolyakov, W. Frias, I.D. Kaganovich, Y. Raitses, Phys. Rev. Lett. **111**, 115002 (2013)
17. D. Sydorenko, A. Smolyakov, I. Kaganovich, Y. Raitses, Phys. Plasmas **14**, 013508 (2007)
18. F. Taccogna, S. Longo, M. Capitelli, R. Schneider, Contrib. Plasm. Phys. **48**, 375 (2008)
19. A. Aanesland, J. Bredin, P. Chabert, V. Godyak, Appl. Phys. Lett. **100**, 044102 (2012)
20. U. Fantz, L. Schiesko, D.W. Wünderlich, Plasma Sources Sci. Technol. **23**, 044002 (2014)
21. A. Shagayda, Phys. Plasmas **19**, 083503 (2012)
22. V.Y. Fedotov, A.A. Ivanov, G. Guerrini, A.N. Vesselovzorov, M. Bacal, Phys. Plasmas **6**, 4360 (1999)
23. X.L. Zhang, R.S. Fletcher, S.L. Rolston, Phys. Rev. Lett. **101**, 195002 (2008)
24. J.P. Boeuf, Frontiers Phys. **2**, 00074 (2014)
25. A. Ducrocq, J.C. Adam, A. Héron, G. Laval, Phys. Plasmas **13**, 102111 (2006)
26. S. Tsikata, T. Minea, Phys. Rev. Lett. **114**, 185001 (2015)
27. V.A. Godyak, R.B. Piejak, Phys. Rev. Lett. **65**, 996 (1990)
28. S. Wilczek, J. Trieschmann, J. Schulze, E. Schuengel, R.P. Brinkmann, A. Derzsi, I. Korolov, Z. Donk, T. Mussenbrock, Plasma Sources Sci. Technol. **24**, 024002 (2015)
29. S. Wilczek, J. Trieschmann, D. Eremin, R.P. Brinkmann, J. Schulze, E. Schuengel, A. Derzsi, I. Korolov, P. Hartmann, Z. Donkó, T. Mussenbrock, Phys. Plasmas **23**, 063514 (2016)
30. I.D. Kaganovich, V.I. Kolobov, L.D. Tsendin, Appl. Phys. Lett. **69**, 3818 (1996)
31. T. Lafleur, P. Chabert, Plasma Sources Sci. Technol. **24**, 044002 (2015)
32. H.C. Lee, M.H. Lee, C.W. Chung, Appl. Phys. Lett. **96**, 041503 (2010)
33. M. Bacal, Rev. Sci. Instrum. **71**, 3981 (2000)
34. N. Oudini, F. Taccogna, A. Bendib, A. Aanesland, Phys. Plasmas **21**, 063515 (2014)
35. N. Oudini, N. Sirse, R. Benallal, F. Taccogna, A. Aanesland, A. Bendib, A.R. Ellingboe, Phys. Plasmas **22**, 073509 (2015)

36. M. Capitelli, R. Celiberto, G. Colonna, F. Esposito, C.G. Hassouni, A. Laricchiuta, S. Longo, *Fundamental aspects of plasma chemical physics* (Springer, 2016)
37. L.D. Pietanza, G. Colonna, G. D'Ammando, A. Laricchiuta, M. Capitelli, Plasma Sources Sci. Technol. **24**, 042002 (2015)
38. Z.L. Petrović, S. Dujko, D. Marić, G. Malović, Ž. Nikitović, O. Šašić, J. Jovanović, V. Stojanović, M. Radmilović-Radjenović, J. Phys. D: Appl. Phys. **42**, 194002 (2009)
39. I. Mann, N. Meyer-Vernet, A. Czechowski, Phys. Rep. **536**, 1 (2014)
40. M. Chaudhuri, A.V. Ivlev, S.A. Khrapak, H.M. Thomas, G.E. Morfill, Soft Matter **7**, 1287 (2011)
41. S.I. Krasheninnikov, R.D. Smirnov, A.Y. Pigarov, T.K. Soboleva, D.A. Mendis, J. Plasma Phys. **76**, 377 (2010)
42. L. Boufendi, A. Bouchoule, Plasma Sources Sci. Technol. **11**, A211 (2002)
43. N. Bilik, R. Anthony, B.A. Merritt, E.S. Aydil, U.R. Kortshagen, J. Phys. D: Appl. Phys. **48**, 105204 (2015)
44. I.B. Denysenko, H. Kersten, N.A. Azarenkov, Phys. Rev. E **92**, 033102 (2015)
45. F. Iza, G.J. Kim, S.M. Lee, J.K. Lee, J.L. Walsh, Y.T. Zhang, M. Kong, Plasma Processes Polymers **5**, 322 (2008)
46. K.H. Schoenbach, K. Becker, Eur. Phys. J. D **70**, 29 (2016)
47. R.J. Carman, R.P. Mildren, J. Phys. D: Appl. Phys. **33**, L99 (2000)
48. Y. Zhang, W. Jiang, A. Bogaerts, J. Phys. D: Appl. Phys. **47**, 435201 (2014)
49. F. Iza, J.K. Lee, M.G. Kong, Phys. Rev. Lett. **99**, 075004 (2007)
50. S.Q. Liu, H. Chen, Phys. Plasmas **19**, 012303 (2012)
51. S.K. Mishra, S. Misra, Phys. Plasmas **21**, 073706 (2014)
52. E. Ahedo, Plasma Physics Controlled Fusion **53**, 124037 (2011)
53. S. Mazouffre, V. Kulaev, J.P. Luna, Plasma Sources Sci. Technol. **18**, 034022 (2009)
54. G. Bourgeois, S. Mazouffre, N. Sadeghi, Phys. Plasmas **17**, 113502 (2010)
55. I.G. Mikellides, I. Katz, R.A. Kuharski, M.J. Mandell, J. Propul. Power **21**, 111 (2005)
56. L.B. King, A.D. Gallimore, J. Propul. Power **20**, 228 (2004)
57. F. Taccogna, S. Longo, M. Capitelli, Eur. Phys. J.: Appl. Phys. **22**, 29 (2003)
58. F. Taccogna, Contrib. Plasm. Phys. **52**, 744 (2012)
59. F. Galli, M. Mamunuru, U.R. Kortshagen, Plasma Sources Sci. Technol. **21**, 035002 (2012)
60. T. Mussenbrock, Contrib. Plasm. Phys. **52**, 571 (2012)
61. D.H. Kang, D.K. Lee, K.B. Kim, J.J. Lee, J. Joo, Appl. Phys. Lett. **84**, 3283 (2004)
62. E. Schüngel, D. Eremin, J. Schulze, T. Mussenbrock, U. Czarnetzki, J. Appl. Phys. **112**, 053302 (2012)
63. A. Derzsi, T. Lafleur, J.P. Booth, I. Korolov, Z. Donkó, Plasma Sources Sci. Technol. **25**, 015004 (2016)
64. P. Diomede, D.J. Economou, T. Lafleur, J.P. Booth, S. Longo, Plasma Sources Sci. Technol. **23**, 065049 (2014)
65. E. Schüngel, Z. Donkó, P. Hartmann, A. Derzsi, I. Korolov, J. Schulze, Plasma Sources Sci. Technol. **24**, 045013 (2015)
66. B. Berger, S. Brandt, J. Franek, E. Schüngel, M. Koepke, T. Mussenbrock, J. Schulze, J. Appl. Phys. **118**, 223302 (2015)
67. J. Trieschmann, M. Shihab, D. Szeremley, A.E. Elgendy, S. Gallian, D. Ermin, R.P. Brinkmann, T. Mussenbrock, J. Phys. D: Appl. Phys. **46**, 084016 (2013)
68. F. Taccogna, P. Minelli, P. Diomede, S. Longo, M. Capitelli, R. Schneider, Plasma Sources Sci. Technol. **20**, 024009 (2011)
69. A. Aanesland, A. Meige, P. Chabert, J. Phys.: Conf. Ser. **162**, 012009 (2009)
70. H.W. Lee, G.Y. Park, Y.S. Seo, Y.H. Im, S.B. Shim, H.J. Lee, J. Phys. D: Appl. Phys. **44**, 053001 (2011)
71. D.J. Economou, Appl. Surf. Sci. **253**, 6672 (2007)
72. M. Bacal, M. Wada, Appl. Phys. Rev. **2**, 021305 (2015)
73. P. Chabert, T.E. Sheridan, J. Phys. D: Appl. Phys. **33**, 1854 (2000)
74. U. Fantz, P. Franzen, D. Wünderlich, Chem. Phys. **398**, 7 (2012)
75. N. Kohen, Ph.D. thesis, Université Toulouse 3 Paul Sabatier, 2015
76. A. Fidman, *Plasma Chemistry* (Cambridge University Press, 2008)
77. *Nonequilibrium Vibrational Kinetics*, edited by M. Capitelli (Springer-Verlag, 1986)
78. V. Laporta, R. Celiberto, J.M. Wadehra, Plasma Sources Sci. Technol. **21**, 055018 (2012)
79. V. Laporta, D.A. Little, R. Celiberto, J. Tennyson, Plasma Sources Sci. Technol. **23**, 065002 (2014)
80. M. Rutigliano, A. Pieretti, M. Cacciatore, N. Sanna, V. Barone, Surf. Sci. **600**, 4239 (2006)
81. R. Celiberto, R. Janev, A. Laricchiuta, M. Capitelli, J. Wadehra, D. Atems, At. Data Nucl. Data Tables **77**, 161 (2001)
82. G. Billing, E. Fisher, Chem. Phys. **43**, 395 (1979)
83. V. Doroshenko, N. Kudryavtsev, S. Novikov, V. Smetanin, High Temperature **28**, 70 (1990)
84. D. Giordano, V. Bellucci, G. Colonna, M. Capitelli, I. Armenise, C. Bruno, J. Thermophys. Heat Transf. **11**, 27 (1997)
85. I. Armenise, F. Esposito, Chem. Phys. **446**, 30 (2015)
86. F. Esposito, I. Armenise, M. Capitelli, Chem. Phys. **331**, 1 (2006)
87. http://phys4entrydb.ba.imip.cnr.it/Phys4EntryDB/
88. C. Treanor, J. Rich, R. Rehm, J. Chem. Phys. **48**, 1798 (1968)
89. W. Urban, J.X. Lin, V. Subramaniam, M. Havenith, J. Rich, Chem. Phys. **130**, 389 (1989)
90. I. Adamovich, S. Saupe, M. Grassi, O. Schulz, S. Macheret, J. Rich., Chem. Phys. **173**, 491 (1993)
91. S. De Benedictis, G. Dilecce, M. Simek, J. Chem. Phys. **110**, 2947 (1999)
92. P. Supiot, D. Blois, S. De Benedictis, G. Dilecce, M. Barj, A. Chapput, O. Dessaux, P. Goudmand, J. Phys. D: Appl. Phys. **32**, 1887 (1999)
93. P.A. Sá, V. Guerra, J. Loureiro, N. Sadeghi, J. Phys. D: Appl. Phys. **37**, 221 (2004)
94. V. Laporta, J. Tennyson, R. Celiberto, Plasma Sources Sci. Technol. **25**, 06LT02 (2016)
95. M. Bacal, Nucl. Fusion **46**, S250 (2006)

96. M. Hopkins, K. Mellon, Phys. Rev. Lett. **67**, 449 (1991)
97. M. Bacal, Chem. Phys. **398**, 3 (2012)
98. A. Bogaerts, T. Kozak, K. van Laer, R. Snoeckx, Faraday Discuss. **183**, 217 (2015)
99. T. Kozak, A. Bogaerts, Plasma Sources Sci. Technol. **23**, 045004 (2014)
100. T. Kozak, A. Bogaerts, Plasma Sources Sci. Technol. **24**, 015024 (2015)
101. R. Aerts, T. Martens, A. Bogaerts, J. Phys. Chem. C **116**, 23257 (2012)
102. L.D. Pietanza, Chem. Phys. **468**, 44 (2016)
103. I. Armenise, E.V. Kustova, Chem. Phys. **415**, 269 (2013)
104. L.M. Martini, G. Dilecce, M. Scotoni, P. Tosi, S. De Benedictis, Plasma Process. Polym. **11**, 232 (2014)
105. M. Lieberman, A. Lichtenberg, *Principles of plasma discharges and materials processing* (Wiley-Interscience, 1994)
106. X. Lu, G.V. Naidis, M. Laroussi, S. Reuter, D.B. Graves, K. Ostrikov, Phys. Rep. **630**, 1 (2016)
107. A. Starikovskiy, N. Aleksandrov, Prog. Energy Combust. Sci. **39**, 61 (2013)
108. Y. Ju, W. Sun, Prog. Energy Combust. Sci. **48**, 21 (2015)
109. J. Van Durme, J. Dewulf, C. Leys, H. Van Langehowe, Appl. Catal. B: Environ. **78**, 324 (2008)
110. M. Golde, Int. J. Chem. Kin. **20**, 75 (1988)
111. U. Kogelschatz, Plasma Chem. Plasma Process. **23**, 1 (2003)
112. G.D. Stancu, F. Kaddouri, D.A. Lacoste, C.O. Laux, J. Phys. D: Appl. Phys. **43**, 124002 (2010)
113. H. Chen, H. Lee, M. Chang, Plasma Process. Polym. **3**, 682 (2006)
114. F. Massines, N. Gherardi, N. Naudé, P. Segur, Plasma Phys. Control. Fusion **47**, B577 (2005)
115. G. Dilecce, P.F. Ambrico, S. De Benedictis, Plasma Sources Sci. Technol. **16**, 511 (2007)
116. G. Colonna, A. D'Angola, *Plasma Modeling: Methods and Applications* (Institute of Physics, New York, in press)
117. N.R. Pinhão, Z. Donkó, D. Loffhagen, M.J. Pinheiro, E.A. Richley, Plasma Sources Sci. Technol. **13**, 719 (2004)
118. G.J.M. Hagelaar, L.C. Pitchford, Plasma Sources Sci. Technol. **14**, 722 (2005)
119. S. Dujko, R.D. White, Z.L. Petrović, R.E. Robson, Plasma Sources Sci. Technol. **20**, 024013 (2011)
120. G.K. Grubert, D. Loffhagen, J. Phys. D: Appl. Phys. **47**, 025204 (2014)
121. L.C. Pitchford, A.V. Phelps, Phys. Rev. A **25**, 540 (1982)
122. W.L. Morgan, *Elendif for windows 9x/nt/2000/xp: The boltzmann equation solver*, http://kinema.com/elendif/ (2010)
123. N. R. Pinhão, *PLASMAKIN: a chemical kinetics package*, http://sourceforge.net/projects/plasmakin/ (2010)
124. G.H.M. Hagelaar, *BOLSIG+ Electron Boltzmann equation solver*, http://www.bolsig.laplace.univ-tlse.fr/ (2010)
125. M. Capitelli, I. Armenise, D. Bruno, M. Cacciatore, R. Celiberto, G. Colonna, O. De Pascale, P. Diomede, F. Esposito, C. Gorse, K. Hassouni, A. Laricchiuta, S. Longo, D. Pagano, D. Pietanza, M. Rutigliano, Plasma Sources Sci. Technol. **16**, S30 (2007)
126. G. Colonna, G. D'Ammando, L.D. Pietanza, M. Capitelli, Plasma Physics Controlled Fusion **57**, 014009 (2015)
127. R.W. Hockney, J.W. Eastwood, *Computer simulation using particles* (IOP Publishing Ltd, 1989)
128. K. Nanbu, IEEE Trans. Plasma Sci. **28**, 971 (2000)
129. C.K. Birdsall, A.B. Langdon, *Plasma physics via computer simulation* (Taylor and Francis, 2005)
130. J.M. Dawson, Rev. Mod. Phys. **55**, 403 (1983)
131. J.P. Verboncoeur, Plasma Physics Controlled Fusion **47**, A231 (2005)
132. D. Tskhakaya, K. Matyash, R. Schneider, F. Taccogna, Contrib. Plasm. Phys. **47**, 563 (2007)
133. V. Vahedi, M. Surendra, Comput. Phys. Commun. **87**, 179 (1995)
134. C. Wang, T. Lin, R. Caflisch, B.I. Cohen, A.M. Dimits, J. Comput. Phys. **227**, 4308 (2008)
135. Y.M. Li, L.C. Pitchford, T.J. Moratz, Appl. Phys. Lett. **54**, 1403 (1989)
136. M.A. Furman, M.T.F. Pivi, Phys. Rev. ST Accel. Beams **5**, 124404 (2002)
137. R.D. Falgout, J.E. Jones, U.M. Yang, *High performance preconditioners*, http://computation.llnl.gov/project/linear_solvers/software.php (2015)
138. J.C. Adams, P.N. Swarztrauber, R. Sweet, *Fishpack - efficient fortran subprograms for the solution of separable elliptic partial differential equations*, https://www2.cisl.ucar.edu/resources/legacy/fishpack (2011)
139. X.S. Li, J. Demmel, J. Gilbert, L. Grigori, P. Sao, M. Shao, I. Yamazaki, *Superlu*, http://crd-legacy.lbl.gov/~xiaoye/SuperLU/ (2015)
140. S. Balay, S. Abhyankar, M. Adams, J. Brown, P.B.K. Buschelman, L. Dalcin, V. Eijkhout, W.D. Gropp, D. Kaushik, M.G. Knepley, L.C. McInnes, K. Rupp, B.F. Smith, S. Zampini, H. Zhang, *Portable, extensible toolkit for scientific computation*, http://www.mcs.anl.gov/petsc (2015)
141. A. Gupta, H. Avron, *Watson sparse matrix package (wsmp)*, http://www.research.ibm.com/projects/wsmp (2015)
142. C. Meierbachtol, A. Greenwood, J. Verboncoeur, B. Shanker, IEEE Trans. Plasma Sci. **43**, 3778 (2015)
143. B.W. Yu, S.L. Girshick, J. Appl. Phys. **69**, 656 (1991)
144. Z. Donkó, J. Phys. A: Math. Theor. **42**, 214029 (2009)
145. A. Fierro, J. Dickens, A. Neuber, Phys. Plasmas **21**, 123504 (2014)
146. A. Vapirev, J. Deca, G. Lapenta, S. Markidis, I. Hur, J.L. Cambier, Concurr. Comput.: Pract. Exper. **27**, 581 (2015)
147. V.I. Demidov, S.V. Ratynskaia, K. Rypdal, Rev. Sci. Instrum. **73**, 3409 (2002)
148. V.A. Godyak, V.I. Demidov, J. Phys. D: Appl. Phys. **44**, 233001 (2011)
149. S. Ratynskaia, G. Dilecce, P. Tolias, J. Plasma Phys. **81**, 345810202 (2015)
150. G. Dilecce, M. Capitelli, S. De Benedictis, J. Appl. Phys. **69**, 121 (1991)
151. T. Hoder, M. Černák, J. Paillol, D. Loffhagen, R. Brandenburg, Phys. Rev. E **86**, 055401(R) (2012)
152. G. Dilecce, Plasma Sources Sci. Technol. **23**, 015011 (2014)
153. X.M. Zhu, Y.K. Pu, J. Phys. D: Appl. Phys. **43**, 015204 (2010)

154. X.M. Zhu, J.L. Walsh, W.C. Chen, Y.K. Pu, J. Phys. D: Appl. Phys. **45**, 295201 (2012)
155. R. Winkler, D. Loffhagen, F. Sigeneger, Appl. Surf. Sci. **192**, 50 (2002)
156. S. Ratynskaia, G. Dilecce, P. Tolias, Appl. Phys. A **117**, 409 (2014)
157. E. Carbone, S. Nijdam, Plasma Phys. Controlled Fusion **57**, 014026 (2015)
158. S. Hübner, J. Sousa, J. van der Mullen, W. Graham, Plasma Sources Sci. Technol. **24**, 10 (2015)
159. H.J. van der Meiden, Plasma Phys. Controlled Fusion **52**, 045009 (2010)
160. H.J. van der Meiden, A.R. Lof, M.A. van den Berg, S. Brons, A.J.H. Donné, H.J.N. van Eck, P.M.J. Koelman, W.R. Koppers, O.G. Kruijt, N.N. Naumenko, T. Oyevaar, P.R. Prins, J. Rapp, J. Scholten, D.C. Schram, P.H. M. Smeets, G. van der Star, S.N. Tugarinov, P.A. Zeijlmans van Emmichoven, Rev. Sci. Instrum. **83**, 123505 (2012)
161. D.E. Evans, J. Katzenstein, Rep. Prog. Phys. **1969**, 207 (1969)
162. D. Froula, S. Glentzer, N. Luhmann Jr., J. Sheffield, *Plasma scattering of electromagnetic radiation: theory and measurement techniques* (Academic Press, 2011)
163. E.A.D. Carbone, S. Hubner, J.M. Palomares, J.J.A.M. van der Mullen, J. Phys. D: Appl. Phys. **45**, 345203 (2012)
164. E.A.D. Carbone, S. Hubner, M. Jimenez-Diaz, J.M. Palomares, E. Iordanova, W.A.A.D. Graef, A. Gamero, J.J.A.M. van der Mullen, J. Phys. D: Appl. Phys. **45**, 475202 (2012)
165. E.V. Barnat, K. Frederickson, Plasma Sources Sci. Technol. **19**, 055015 (2010)
166. G. Dilecce, P.F. Ambrico, S. De Benedictis, J. Phys. B **28**, 209 (1995)
167. E.A. Den Hartog, T.R. O'Brian, J.E. Lawler, Phys. Rev. Lett. **62**, 1500 (1989)
168. K.P. Horn, P. Ottinger, J. Chem. Phys. **54**, 3040 (1971)
169. S. De Benedictis, R. D'Agostino, F. Cramarossa, Chem. Phys. **71**, 247 (1982)
170. S. De Benedictis, M. Capitelli, F. Cramarossa, R. D'Agostino, C. Gorse, Chem. Phys. Lett. **112**, 54 (1984)
171. G. Dilecce, S. De Benedictis, *NO(X, v) distributions in rf discharges: conditions for a very high vibrational pumping*, in *Proc. XII International Symposium on Plasma Chemistry (ISPC) – Minneapolis*, edited by J. Heberlein, D. Ernie, J. Roberts (1995), pp. 403–408
172. N. Legay-Sommaire, F. Legay, Can. J. Phys. **48**, 1966 (1969)
173. D. Marinov, D. Lopatik, O. Guaitella, Y. Ionikh, J. Ropcke, A. Rousseau, J. Phys. D: Appl. Phys. **47**, 015203 (2014)
174. S. De Benedictis, G. Dilecce, Chem. Phys. **192**, 149 (1995)
175. S. De Benedictis, G. Dilecce, J. Phys. B **27**, 615 (1994)
176. M. Foucher, D. Marinov, E. Carbone, P. Chabert, J.P. Booth, Plasma Sources Sci. Technol. **24**, 042001 (2015)
177. W. Demtröder, *Laser Spectroscopy* (Springer, 2003)
178. A. Lo, G. Cléon, P. Vervish, A. Cessou, Appl. Phys. B **107**, 229 (2012)
179. A. Lo, A. Cessou, P. Boubert, P. Vervisch, J. Phys. D: Appl. Phys. **47**, 115201 (2014)
180. W.R. Lempert, I.V. Adamovich, J. Phys. D: Appl. Phys. **47**, 433001 (2014)
181. A. Montello, Z. Yin, D. Burnette, I.V. Adamovich, W.R. Lempert, J. Phys. D: Appl. Phys. **46**, 464002 (2013)
182. B. Massabieaux, G. Gousset, M. Lefebvre, M. Péalat, J. Phys. France **48**, 1939 (1987)
183. M. Péalat, J.E. Taran, M. Bacal, F. Hillion, J. Chem. Phys. **82**, 4943 (1985)
184. H.J. Kunze, *Introduction to Plasma Spectroscopy* (Springer, 2009)
185. S. Reuter, Plasma Sources Sci. Technol. **24**, 054001 (2015)
186. G. Dilecce, P.F. Ambrico, M. Simek, S. De Benedictis, J. Phys. D: Appl. Phys. **45**, 125203 (2012)
187. G. Cunge, D. Vempaire, M. Touzeau, N. Sadeghi, Appl. Phys. Lett. **91**, 231503 (2007)
188. M.H. Loh, M.A. Cappelli, Appl. Phys. Lett. **70**, 1052 (1997)
189. P. Bruggeman, G. Cunge, N. Sadeghi, Plasma Sources Sci. Technol. **21**, 035019 (2012)
190. *Cavity-Enhanced Spectroscopy and sensing*, edited by G. Gagliardi, H.P. Loock, Vol. 179 of *Springer Series in Optical Sciences* (Springer Berlin Heidelberg, 2014)
191. J. Ropcke, P.B. Davies, N. Lang, A. Rousseau, S. Welzel, J. Phys. D: Appl. Phys. **45**, 423001 (2012)
192. S.E. Fiedler, A. Hese, A.A. Ruth, Chem. Phys. Lett. **371**, 284 (2003)
193. I. Ventrillard-Courtillot, E. Sciamma O'Brien, S. Kassi, G. Méjean, D. Romanini, Appl. Phys. B **101**, 661 (2010)
194. A. O'Keefe, D. Deacon, Rev. Sci. Instrum. **59**, 2544 (1988)
195. *Cavity Ring-Down Spectroscopy: Techniques and Applications*, edited by G. Berden, R. Engeln (Wiley-Blackwell, 2009)
196. S.M. Ball, R.L. Jones, Chem. Rev. **103**, 5239 (2003)
197. B. Bakowski, G. Hancock, R. Peverall, G.A.D. Ritchie, L.J. Thornton, J. Phys. D: Appl. Phys. **37**, 2064 (2004)
198. G. Hancock, R. Peverall, G.A.D. Ritchie, L.J. Thornton, J. Phys. D: Appl. Phys. **39**, 1846 (2006)
199. G.D. Stancu, M. Janda, F. Kaddouri, D.A. Lacoste, C.O. Laux, J. Phys. Chem. A **114**, 201 (2010)
200. C. Wang, N. Srivastava, S. Scherrer, P.R. Jang, T.S. Dibble, Y. Duan, Plasma Sources Sci. Technol. **18**, 025030 (2009)
201. Z.W. Liu, X.F. Yang, A.M. Zhu, G.L. Zhao, Y. Xu, Eur. Phys. J. D **48**, 365 (2008)
202. S. Williams, M. Gupta, T. Owano, D.S. Baer, A. O'Keefe, D.R. Yarkony, S. Matsika, Opt. Lett. **29**, 1066 (2004)
203. T. Ombrello, S.H. Won, Y. Ju, S. Williams, Combust. Flame **157**, 1916 (2010)
204. R. Zaplotnik, M. Bišćan, N. Krstulović, D. Popović, S. Milošević, Plasma Sources Sci. Technol. **24**, 054004 (2015)
205. C. Hibert, I. Gaurand, O. Motret, J.M. Pouvesle, J. Appl. Phys. **85**, 7070 (1999)
206. G. Dilecce, L.M. Martini, P. Tosi, M. Scotoni, S. De Benedictis, Plasma Sources Sci. Technol. **24**, 034007 (2015)
207. K. Niemi, V.S. von der Gathen, H.F. Döbele, J. Phys. D: Appl. Phys. **34**, 2330 (2001)

208. K. Niemi, V.S. von der Gathen, H.F. Döbele, Plasma Sources Sci. Technol. **14**, 375 (2005)
209. H.F. Döbele, T. Mosbach, K. Niemi, V.S. von der Gathen, Plasma Sources Sci. Technol. **14**, S31 (2005)
210. R. Loudon, *The Quantum Theory of Light* (Clarendon, Oxford, 1983)
211. P. Pezé, A. Paillous, J. Siffre, B. Dubreuil, J. Phys. D: Appl. Phys. **26**, 1622 (1993)
212. J. Amorim, G. Baravian, M. Touzeau, J. Jolly, J. Appl. Phys. **76**, 1487 (1994)
213. S. De Benedictis, G. Dilecce, in *Low Temperature Plasma Technology: Methods and Applications*, edited by P.K. Chu, X.P. Lu (CRC Press, Boca Raton, London, New York, 2013), pp. 261–284
214. S. Samukawa, M. Hori, S. Rauf, K. Tachibana, P. Bruggeman, G. Kroesen, J.C. Whitehead, A.B. Murphy, A.F. Gutsol, S. Starikovskaia, U. Kortshagen, J.-P. Boeuf, T.J. Sommerer, M.J. Kushner, U. Czarnetzki, N. Mason, J. Phys. D: Appl. Phys. **45**, 253001 (2012)